Electromagnetics of waveguides, scattering, and MRI systems

A DISSERTATION
SUBMITTED TO THE FACULTY OF THE GRADUATE SCHOOL
OF THE UNIVERSITY OF MINNESOTA
BY

HYOUNGSUK YOO

IN PARTIAL FULFILLMENT OF THE REQUIREMENTS
FOR THE DEGREE OF
DOCTOR OF PHILOSOPHY

Anand Gopinath, Ph.D.

October 2009

Acknowledgments

I would like to express my sincere appreciation to my advisor, Dr. Anand Gopinath for his endless encouragement, valuable guidance, and financial support throughout all stages of my Ph.D. studies and research at the University of Minnesota. I would also like to thank Dr. Tommy Vaughan for his guidance and support of this work.

My thanks also go to current and former members of our research group. In addition, I would like to thank my friends at this University and elsewhere for their assistance and encouragement to continue my studies.

I would like to give special thanks to both my parents, Suchan Yoo and Yongsun Lee, and parents in law for their loves, encouragements, and constant supports to continue my studies because without them this work would not have been possible. My deepest gratitude goes to my grandmother in heaven for her endless love and care.

Finally, I would like to thank my lovable wife, Juhyun Park and my adorable son, Jaehee Yoo for their sacrificial love and support during these years of study. I will never be able to thank my family enough.

Abstract

The vector finite-element method in the interior and the boundary integral equation of the exterior domain are investigated in order to analyze open dielectric waveguides. Boundary conditions are obtained by applying the continuity of the magnetic and electric fields at the surface of the waveguide. Since both the finite-element method and boundary integral equations have the final matrices of the form $Ax = \lambda Bx$, the singular value decomposition method with iterations is used. This method provides excellent accurate solutions for a rectangular dielectric waveguides. The zero cutoff of the lowest order mode is also obtained. To avoid iterations, the finite-element formulation together with the boundary operator are solved using a penalty function method. Comparison with previously published results shows good agreement for the analysis of the rectangular dielectric waveguide. Finally, the pseudoinverse method with a penalty factor is used. This new method provides the simultaneous solutions of propagating modes at the operating frequency and it shows good agreement with previously published results for the analysis of the rectangular waveguide.

The electromagnetic scattering problem by surfaces of arbitrary objects is discussed based on the method of moments technique and surface integral equations. Similar to the case of the conducting scatterers, the arbitrary geometrical shapes have been modeled using triangulated patches when combined field integral formulations are developed for the scattering by dielectric objects. The treatment of singular integral equations is also mentioned and the results for the metal plate are compared for it. The approach is applied to the scattering problems of plane wave illumination of a dielectric finite circular cylinder and a cubic high dielectric resonator. Scattered fields are evaluated after determining the surface electric and magnetic currents as unknowns for the high dielectric cube to find the magnetic and electric dipole inside the cube.

The higher magnetic B_0 fields in MRI systems result in higher signal to noise ratios. However, as the wavelength decreases linearly with higher static magnetic field, image inhomogeneity occurs. This thesis demonstrates the use of the convex optimization with an

iterative method to improve B_1^+ uniformity in an anatomic region of interest by varying the magnitude and phase of each RF channel element independently. The simulation results for 16 and 32 channels for 9.4T and 7T systems and experimental results for 8 channels in a 9.4T system confirming the prediction are presented.

Contents

List of Tables

List of Figures

Chapter 1

Introduction

1.1 Overview

This thesis consists of studies of three different research areas: (1) analysis of open dielectric waveguide using the finite element method, (2) electromagnetic scattering by dielectric objects using the method of moments, and (3) RF B_1 field localization in high magnetic field systems through the convex optimization. Initially, the motivation for these projects is given together with a summary of the approaches adopted, followed by an outline of the thesis.

1.2 Motivation and Summary

1.2.1 Finite Element Method for Analysis of Open Waveguides

Most commercial software uses the beam propagation method (BPM) for modeling integrated and fiber optic devices. For the modal properties of the optical waveguide, the imaginary distance BPM does not work well with high contrast, and small waveguides. So-

lution to this problem is to use the finite-element method, but this requires an enclosure of either perfect electric or magnetic walls or an enclosure by absorbing boundaries or perfectly matched layers. The problem with these approaches is that the walls need to be sufficiently far from the dielectric waveguide so as not to perturb the modes. Thus, the analyzed guide structure cross section is large, and the dielectric guide mode number is large, which causes a reduction in the accuracy of the eigenvalue and corresponding eigenvectors.

The combination of the finite-element method (FEM) and boundary-integral equations (BIE) is utilized to overcome above disadvantages for modal solutions. In this thesis, the finite-element method with edge elements and boundary integral equations are used to solve the open dielectric waveguide problem. The wave equation results in the generalized eigenvalue equation which has full rank matrix and the propagation constant β^2 as the eigenvalues. Since only the natural boundary condition is represented in the wave equation, it is necessary to use Green's theorem to relate the exterior region fields to the interior region fields and then impose boundary conditions at the interface which require that the tangential E and H fields are continuous. The solution is obtained by three new methods and these methods provide accurate solutions for the propagation constants of the modes of the open rectangular dielectric waveguide.

1.2.2 Method of Moments for Scattering by Dielectric Objects

There are a variety of numerical methods for electromagnetic scattering by dielectric objects. Depending on the dimensions of the problem is formulated, numerical methods are divided into volumetric and surface methods. The finite element method and the finite difference time domain method are volumetric methods and they need to discretize the entire computational domain. The computational costs increase when fine meshes are required for

accuracy. For arbitrary shaped objects, the combined field surface integral equation (CFIE) with method of moments is well suited to analyzing homogeneous dielectric scatterers. This technique may be used to analyze radio-freqeuncy (RF) coil arrays in high field magnetic resonance imaging (MRI) because the CFIE method offers great modelling flexibility and solution accuracy for arbitrarily shaped coils, phantoms and the human body.

To analyze electromagnetic scattering by arbitrary shaped three dimensional homogeneous lossy and lossless objects, the combined field integral formulation is used. In the method of moments formulation, triangular surface patches with the Rao-Wilton-Glisson (RWG) current basis functions are used to model arbitrarily shaped geometries. This technique provides the equivalent surface current distributions generated from plane wave scattering from a dielectric finite circular cylinder. The scattered fields, both internal and external, for a cubic high dielectric resonator are obtained after solving the combined field integral equations to verify magnetic and electric dipoles at resonant modes. This method may be extended for MRI applications by modelling RF coils and loaded with phantoms and the human body.

1.2.3 RF B_1 Field Localization in High Magnetic Field Systems

High magnetic field magnetic resonance imaging scanners with static B_0 magnetic fields of 4T, 7T and 9.4T improve the signal to noise ratios (SNR). However, the transverse radio frequency magnetic B_1 field non-uniformity also occurs due to the increased RF field frequencies when wavelengths in human anatomy become shorter than its size. Since MRI applications require homogeneous B_1^+, which is the circularly-polarized component of the RF B_1 magnetic field, in the subject, many approaches have been investigated to minimize B_1^+ non-uniformity. In particular, multi-channel coils for the parallel imaging have received

a remarkable amount of interest and investigated in high magnetic field systems, because they provide high local SNR, which can be used for parallel imaging. However, destructive B_1^+ interference patterns also occur when the multi-channel transmission line also called the transverse electromagnetic (TEM) coil, is used.

To control the RF field in high magnetic field systems, the control of the amplitude and phase of individual coil elements may be used to develop a desired B_1^+ field distribution. The choice of the excitation parameter of the coil elements is determined by convex optimization. Convex optimization is used to provide optimal results rapidly, when the problem is formulated globally. In addition, convex optimization provides better signal to noise (SNR) ratio when anatomic specific regions are investigated. Although the general convex optimization shows these advantages, problems remain, including high field distribution at the edges and non-homogeneity in suppression region. In this thesis, a better approach is demonstrated with an iterative method, which makes this method more useful. Simulation results are compared for 7T and 9.4T systems based on the number of elements. An experiment was performed using an eight channel transmission line coil, and the results confirm the theoretical prediction.

1.3 Outline of the Thesis

Chapter 1 has provided an introduction to the projects performed for this thesis.

In chapter 2 of the thesis, the finite element method (FEM) and boundary integral equations (BIE) developed from the Green's theorem for analysis of open dielectric are discussed. Both FEM and BIE approaches have the final matrices of form $Ax = \beta^2 Bx$, where β is the propagation constant, and the procedures to find the modal solutions are different. Three different methods to solve the FEM-BIE equation are proposed. These

methods are: (1) iterative method with singular value decomposition; (2) penalty function method; (3) pseudoinverse method. The results obtained with these techniques for open square dielectric waveguides compare very well with the previously published solutions.

In chapter 3, the combined electric and magnetic field integral equations are used with the method of moments to develop an efficient numerical procedure for analyzing the electromagnetic scattering by surfaces of arbitrary shaped objects. Triangular surface patch models with Rao-Wilton-Glisson (RWG) basis functions are used and the singularities in the solution of the integral equations are treated with appropriate closed form solutions. The method of moments approach discussed in this chapter shows the numerical results for plane wave scattering by a dielectric finite circular cylinder and a cubic high dielectric resonator. The distribution of surface electric and magnetic currents are obtained and the scattered fields are evaluated from the solutions.

Chapter 4 develops RF magnetic B_1 field localization in high magnetic field systems. Mathematical formulation of the localization problem is discussed in detail and convex optimization with iterative method is demonstrated to improve B_1^+ uniformity in an anatomic region of interest by varying the magnitude and phase of each RF channel element independently. Simulation results for 16 and 32 channels are compared for 7T and 9.4T systems based on human head and phantom model. Hardware setup for the 9.4T system is briefly introduced and experimental results for 8 channels confirm the prediction are presented.

Finally, chapter 5 concludes with a summary of the contributions of this thesis and future research directions.

Chapter 2

Analysis of Open Dielectric Waveguides

2.1 Introduction

Since open waveguides such as optical fibers, unshielded microstrip lines and various dielectric waveguides have gained increasing use, many numerical methods have been investigated for potential applications in optical transmission technologies [1]–[8]. In particular, most commercial software uses the beam propagation method (BPM) for modeling integrated and fiber optic devices [9]. For the modal properties of the optical waveguide, the imaginary distance BPM does not work well with high contrast waveguides. Solution to this is to use the finite-element method, but this requires an enclosure of either perfect electric or magnetic walls. The problem with this approach is that the walls need to be sufficiently far from the dielectric waveguide so as not to perturb the modes. Thus, the analyzed guide structure cross section is large, and the dielectric guide mode number is large, which causes

a reduction in the accuracy of the eigenvalue and corresponding eigenvectors. Here also, the identification of the correct mode requires scanning through several eigenvector modal plots. The more realistic alternative is to use an absorbing or perfectly matched boundary condition, which results in complex eigenvalues and vectors which are non-physical, which is due to these boundary conditions. Su [5] has used transverse H field formulation in the finite-element method with nodal elements, and the frontal method is used in the process of matrix assembling, and the propagation constant is determined in an iterative search procedure. Rogier et al. [7] have developed the transverse and longitudinal H or E field formulation, and imposed the continuity of the tangential H or E field. Similar to [5], they used a modified version of the frontal method which eliminates internal finite-element variables to condense the sparse system. Eliseev et al. paper [8] is a scalar formulation, however, an iterative procedure is required to obtain the dispersion characteristics from the linear generalized eigenvalue problem. In general, these techniques use the nodal based FEM for applying the continuity of E_z or H_z, and these boundary conditions are applied to all regions of interest.

In this thesis, the finite-element method with edge and nodal elements and the boundary integral equations are used to solve the open dielectric waveguide problem. The wave equation as applied to the guide results in the generalized eigenvalue equation which has a full rank matrix and the propagation constant β^2 as the eigenvalues. Since only the natural boundary condition is represented in the wave equation, it is necessary to use Green's theorem to represent the exterior region fields in terms of the interior region fields and then impose boundary conditions at the interface which require that the tangential E and H fields are continuous. This results in a boundary operator matrix, which is rectangular, and also contains the propagation constant β^2. Any solution requires that both the wave

equation matrix and the boundary operator matrix are satisfied simultaneously.

In this chapter, the solution is obtained by three different methods. The first one is an iterative method with the singular value decomposition (SVD) [10], which finds the solutions iteratively until the difference of the trial value and final value converges to a negligibly small value. To avoid iterations, the second method proposed adding the boundary operator matrix to the FEM matrix [11]. This method only added equations for the continuity of the transverse magnetic fields across the open boundaries with a penalty factor. However, the penalty factor needs to be changed for analyzing different modes, and the accuracy is not as high near the cutoff frequencies as the iterative method. Finally, the pseudoinverse method with a penalty factor is used since both the finite-element method and boundary integral equations have the final matrices of the form $Ax = \lambda Bx$ [12]. This new method provides the simultaneous solutions of propagating modes at the operating frequency and eliminates iterations. These three methods are applied for the modal analysis of open rectangular dielectric waveguides, and the solutions are compared with the previous results [2] [3].

2.2 Basic Formulation

To solve the boundary-value problem for the full-wave analysis of open waveguides, it is necessary to start from Maxwell's curl equations for a source free medium:

$$\nabla \times \mathbf{E} = -j\omega\mu\mathbf{H} \tag{2.1}$$

$$\nabla \times \mathbf{H} = j\omega\varepsilon\mathbf{E}. \tag{2.2}$$

For the finite-element method, we substitute (2.2) into (2.1) to obtain the following equation

$$\nabla \times \left(\frac{1}{\varepsilon_r} \nabla \times \mathbf{H} \right) - k_0^2 \mu_r \mathbf{H} = 0 \tag{2.3}$$

where $\mathbf{H} = \widehat{a_x} H_x + \widehat{a_y} H_y + \widehat{a_z} H_z$, k_0 is the wavenumber in free space, ε_r, μ_r are the relative permittivity and permeability, respectively. Using the Galerkin method, multiply equation (2.3) by $\mathbf{H}^*$ and using the vector identity $\nabla \cdot (\mathbf{A} \times \mathbf{B}) = \mathbf{B} \cdot (\nabla \times \mathbf{A}) - \mathbf{A} \cdot (\nabla \times \mathbf{B})$, the boundary equation (2.3) simplifies to

$$\frac{1}{\varepsilon_r} (\nabla \times \mathbf{H}) \cdot (\nabla \times \mathbf{H})^* - k_0^2 \mu_r \mathbf{H} \cdot \mathbf{H}^* - \nabla \cdot [\mathbf{H} \times \frac{1}{\varepsilon_r} (\nabla \times \mathbf{H})^*] = 0. \tag{2.4}$$

Integrating over the surface S which denotes the cross section of the structure at (2.4), gives

$$\int_{\mathrm{S}} \frac{1}{\varepsilon_r} (\nabla \times \mathbf{H}) \cdot (\nabla \times \mathbf{H})^* - k_0^2 \mu_r \mathbf{H} \cdot \mathbf{H}^* dS - \int_{\mathrm{S}} \nabla \cdot [\mathbf{H} \times \frac{1}{\varepsilon_r} (\nabla \times \mathbf{H})^*] dS = 0 \tag{2.5}$$

also

$$\int_{\mathrm{S}} \nabla \cdot [\mathbf{H} \times \frac{1}{\varepsilon_r} (\nabla \times \mathbf{H})^*] dS = \oint_C [\mathbf{H} \times \frac{1}{\varepsilon_r} (\nabla \times \mathbf{H})^*] \cdot \hat{\mathrm{n}} dl \tag{2.6}$$

where C denotes the contour of the surface S, $\hat{\mathrm{n}}$ is the outward unit normal vector to C. The right hand side of (2.6) is the natural boundary condition which represents the complementary Poynting vector $\mathbf{H} \times \mathbf{E}^*$. Therefore, the contour integration in (2.6) can be ignored because no power flow exists outward from the surface of the lossless waveguide for the guided mode. Assuming a known z-dependence as $\mathbf{H}(x, y, z) = \mathbf{H}(x, y) e^{-j\beta z}$, where β is the propagation constant and separating the transverse component x, y and the longitudinal

component z of the del operator, the following can be obtained

$$\nabla = \nabla_t + \hat{z}\frac{\partial}{\partial z} = \nabla_t - i\beta\hat{z} \tag{2.7}$$

and

$$\nabla \times \mathbf{H} = (\nabla_t - i\beta\hat{z}) \times (\mathbf{H}_t + \hat{z}H_z) = (\nabla_t \times \mathbf{H}_t) + (\nabla_t H_z + i\beta\mathbf{H}_t) \times \hat{z}. \tag{2.8}$$

Applying (2.8) to (2.5), (2.5) becomes

$$\int_S \left[\frac{1}{\varepsilon_r}(\nabla_t \times \mathbf{H}_t) \cdot (\nabla_t \times \mathbf{H}_t)^* - k_0^2\mu_r\mathbf{H} \cdot \mathbf{H}^* + \frac{1}{\varepsilon_r}(\nabla_t H_z + i\beta\mathbf{H}_t) \cdot (\nabla_t H_z + i\beta\mathbf{H}_t)^*\right] dS = 0. \tag{2.9}$$

where $\mathbf{H}_t$, H_z denote the transverse and longitudinal magnetic field, respectively. In practice, solving for the propagation constant with the specified operating frequency is preferred. To solve this problem, simple transformations are introduced [13]

$$\mathbf{H}_t = \beta^{-1}\mathbf{h}_t, \quad H_z = ih_z. \tag{2.10}$$

Substituting these variable transformations into (2.9) and multiplying by β^2, the final finite-element formulation is expressed as

$$\int_S \left\{\frac{1}{\varepsilon_r}(\nabla_t \times \mathbf{h}_t) \cdot (\nabla_t \times \mathbf{h}_t)^* - k_0^2\mu_r\mathbf{h}_t \cdot \mathbf{h}_t^* + \beta^2\left[\frac{1}{\varepsilon_r}(\nabla_t h_z + \mathbf{h}_t) \cdot (\nabla_t h_z + \mathbf{h}_t)^* - k_0^2\mu_r h_z h_z^*\right]\right\} ds = 0. \tag{2.11}$$

The above formulation consists of the transverse field $\mathbf{h}_t$ and the longitudinal field h_z and results in an eigenmatrix equation with β^2 as the propagation constant. The finite element method for the solution of this wave equation is discussed next.

2.3 Finite Element Method

The finite element method (FEM) has been used to analyze problems in electromagnetics since 1968 [14], because it is useful in solving differential equations. Basically, the FEM has four steps for analysis of problems: (1) discretizing the solution domain into a finite number of elements, (2) deriving governing equations for a typical element, (3) assembling of all elements in the solution domain, and (4) solving the resulting equations in the system.

2.3.1 Node Based Elements

For the typical triangular element shown in Fig. 2.1, the longitudinal component h_z is expanded using the node-base interpolation functions

$$h_z^e = n_1^e h_{z1}^e + n_2^e h_{z2}^e + n_3^e h_{z3}^e \tag{2.12}$$

where h_{zj}^e denotes the normal field at the j^{th} node within the e^{th} element, linear interpolation functions are

$$n_1^e = \frac{1}{2A}\left[(x_2y_3 - x_3y_2) + (y_2 - y_3)\,x + (x_3 - x_2)\,y\right] \tag{2.13a}$$

$$n_2^e = \frac{1}{2A}\left[(x_3y_1 - x_1y_3) + (y_3 - y_1)\,x + (x_1 - x_3)\,y\right] \tag{2.13b}$$

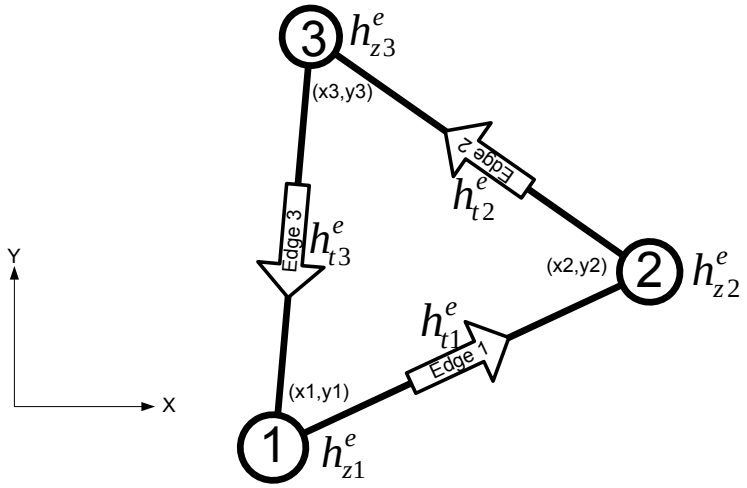

Figure 2.1: Typical triangular element; the local node numbering 1-2-3 must be counterclockwise to keep the triangular area A positive.

$$n_3^e = \frac{1}{2A}\left[(x_1y_2 - x_2y_1) + (y_1 - y_2)\,x + (x_2 - x_1)\,y\right] \tag{2.13c}$$

and A is the area of the triangular element and it can be expressed as at the given x,y coordinates

$$A = \frac{1}{2}\left[(x_2 - x_1)\,(y_3 - y_1) - (x_3 - x_1)\,(y_2 - y_1)\right] \tag{2.14}$$

To keep the value of A positive in (2.14), the nodes numbering must be counterclockwise as shown Fig. 2.1. From (2.12) and (2.13), the interpolation functions have the following properties

$$n_j^e(x_i,y_i) = \begin{cases} 0, & j \neq i \\ 1, & j = i \end{cases} \tag{2.15a}$$

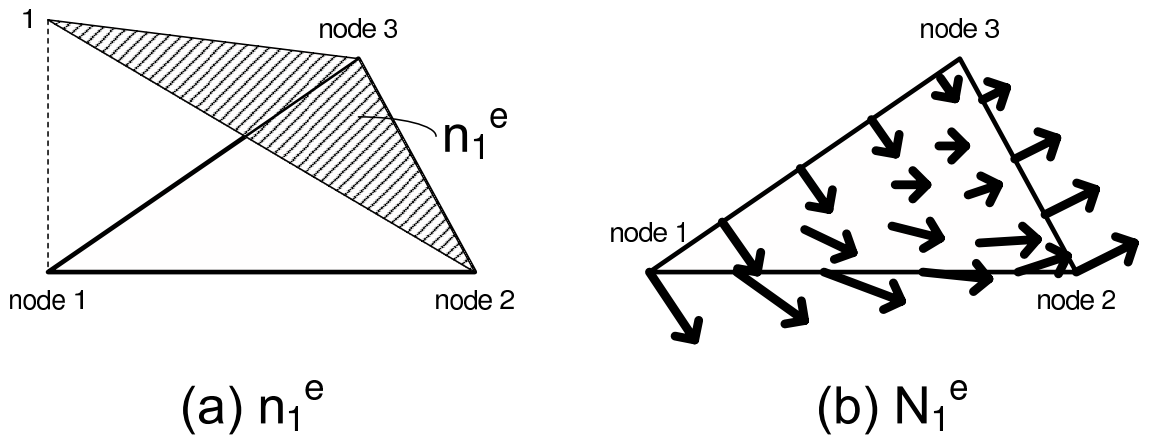

Figure 2.2: Linear node-based and vector basis interpolation functions for a triangular element. (a) n_1^e. (b) $\mathbf{N}_1^e$.

and

$$n_1^e(x,y) + n_2^e(x,y) + n_3^e(x,y) = 1. \tag{2.15b}$$

Since the above equation shows that n_j^e is unity only at the j^{th} node and it decreases linearly then becomes zero at the other nodes, n_j^e is also called the element shape functions (Fig. 2.2 (a)). The longitudinal (or normal) field components are represented by the node-based elements.

2.3.2 Edge Based Elements

The formulation discussed in 2.2 uses all three components of the H field and the normal component of the field, H_z is represented by the usual node-based element. However, for transverse fields this node-base element results in spurious modes especially when calculating the modal properties of mixed dielectric guiding structures. To overcome this disadvantage, vector finite elements or called edge elements are preferred for representing

the transverse field components, and each edge element is based on two nodal elements. In treating the transverse field components, we construct the two-dimensional tangential vector finite element and described mathematically as

$$h_t^e = \mathbf{N}_1^e h_{t1}^e + \mathbf{N}_1^e h_{t2}^e + \mathbf{N}_1^e h_{t3}^e \tag{2.16}$$

where h_{ti}^e denotes the tangential field at the i^{th} edge, $\mathbf{N}_i^e$ are the vector linear interpolation functions, given by

$$\mathbf{N}_1^e = (n_1^e \nabla n_2^e - n_2^e \nabla n_1^e) l_1^e \tag{2.17a}$$

$$\mathbf{N}_2^e = (n_2^e \nabla n_3^e - n_3^e \nabla n_2^e) l_2^e \tag{2.17b}$$

$$\mathbf{N}_3^e = (n_3^e \nabla n_1^e - n_1^e \nabla n_3^e) l_3^e \tag{2.17c}$$

and l_i^e is the length of the i^{th} edge connecting corresponding two nodes and n_i^e are the conventional nodal element. As expected, a vector basis function has a tangential component at the associated edge. Note that these basis functions have a $\hat{x}$ component with y variables and a $\hat{y}$ component with x variables, respectively, from (2.17). These properties are very useful when boundary conditions are imposed with the scalar Green's theorem.

2.3.3 Generalized Eigenvalue Problem

To solve the wave equation (2,11), the cross-sectional area S is subdivided into M small triangular elements. Within each element, the vector transverse field is represented by

$$\mathbf{h}_t^e = \sum_{i=1}^{n} \mathbf{N}_i^e h_{ti}^e = \{\mathbf{N}^e\}^T \{h_t^e\} = \{h_t^e\}^T \{\mathbf{N}^e\} \tag{2.18}$$

where n denotes the number of edges for the element: $n = 3$ for a triangular element. The longitudinal component h_z is represented by the conventional node-based interpolation functions

$$h_z^e = \sum_{i=1}^{n} n_i^e h_{zi}^e = \{n^e\}^T \{h_z^e\} = \{h_z^e\}^T \{n^e\}\,. \tag{2.19}$$

Substituting these into (2,11), the equation becomes:

$$[h_t^e]^T [L_{tt}^e] [h_t^e]^* + \beta^2 \begin{bmatrix} h_t^e \\ h_z^e \end{bmatrix}^T \begin{bmatrix} R_{tt}^e & R_{tz}^e \\ R_{zt}^e & R_{zz}^e \end{bmatrix} \begin{bmatrix} h_t^e \\ h_z^e \end{bmatrix}^* = 0 \tag{2.20a}$$

where the superscript T means a transpose matrix, the asterisk denotes the complex conjugate, and the elemental matrices are given by

$$[L_{tt}^e] = \int_{S^e} \left\{ \frac{1}{\varepsilon_r^e} [\nabla_t \times \mathbf{N}^e] \cdot [\nabla_t \times \mathbf{N}^e]^T - k_0^2 \mu_r^e [\mathbf{N}^e] \cdot [\mathbf{N}^e]^T \right\} ds \tag{2.20b}$$

$$[R_{tt}^e] = \int_{S^e} \frac{1}{\varepsilon_r^e} [\mathbf{N}^e] \cdot [\mathbf{N}^e]^T \, ds \tag{2.20c}$$

$$[R_{tz}^e] = \int_{S^e} \frac{1}{\varepsilon_r^e} [\mathbf{N}^e] \cdot [\nabla_t n^e]^T \, ds \tag{2.20d}$$

$$[R_{zt}^e] = \int_{S^e} \frac{1}{\varepsilon_r^e} [\nabla_t n^e] \cdot [\mathbf{N}^e]^T \, ds \tag{2.20e}$$

$$[R_{zz}^e] = \int_{S^e} \frac{1}{\varepsilon_r^e} [\nabla_t n^e] \cdot [\nabla_t n^e]^T - k_0^2 \mu_r^e [n^e] \cdot [n^e]^T \, ds \tag{2.20f}$$

In the above equations, S^e denotes the area of the triangular element e, with ε_r^e and μ_r^e are the relative permittivity and permeability within the element. Using global notation, (2.20a) is written as

$$[\mathbf{h}_t]^T [L_{tt}] [\mathbf{h}_t]^* + \beta^2 \begin{bmatrix} \mathbf{h}_t \\ h_z \end{bmatrix}^T \begin{bmatrix} R_{tt} & R_{tz} \\ R_{zt} & R_{zz} \end{bmatrix} \begin{bmatrix} \mathbf{h}_t \\ h_z \end{bmatrix}^* = 0 \tag{2.21}$$

The equation (2.21) is also identical to the following generalized eigenvalue problem by applying the Ritz procedure [15]

$$\begin{bmatrix} L_{tt} & 0 \\ 0 & 0 \end{bmatrix} \begin{bmatrix} \mathbf{h}_t \\ h_z \end{bmatrix} = -\beta^2 \begin{bmatrix} R_{tt} & R_{tz} \\ R_{zt} & R_{zz} \end{bmatrix} \begin{bmatrix} \mathbf{h}_t \\ h_z \end{bmatrix}. \tag{2.22}$$

The order of the square matrices $[L]$ and $[R]$ is $(e+n) \times (e+n)$, where e and n are the number of the edges and the nodes, respectively. Since the above equation satisfies the wave equation (2.11) with the natural outer boundary condition, the solution β as an eigenvalue is adequate for the closed waveguide analysis such as shielded microstrip lines, coaxial cables, and wave-guiding structures with metal enclosures. For open waveguides,

the natural boundary condition represented by (2.6) is not adequate, and the continuity of the tangential fields boundary condition needs to be imposed.

2.4 Boundary Integral Equation

2.4.1 Green's Theorem

The finite-element formulations with nodal and edge elements have been derived for the closed waveguide which has the natural outer boundary conditions. In this section, the boundary conditions between the exterior and interior region for open waveguides are derived by the scalar Green's theorem, for all three components. This theorem makes the connection between the exterior fields and the interior fields which are represented by the finite-elements. The scalar Green's second identity may be derived from the Helmholtz partial differential equation and is given by [17]

$$\int_S \left(\varphi\nabla^2\psi - \psi\nabla^2\varphi\right) ds_0 = \oint_C \left(\varphi\frac{\partial\psi}{\partial n} - \psi\frac{\partial\varphi}{\partial n}\right) dr_0 \tag{2.23}$$

and the Helmholtz equation is given as:

$$\nabla^2\varphi(r) + k_0^2\varepsilon_r\varphi(r) = 0 \tag{2.24}$$

where $\hat{n}$ is an outward directed unit vector as shown in Fig. 2.3. Set $\varphi = H_i(r_0)$ where $i = x, y, z$ and $\psi = G(r, r_0)$, the Green's function and r, r_0 denote the source and observation points, respectively. The Green's function $G(r, r_0)$ satisfies the following partial differential equation

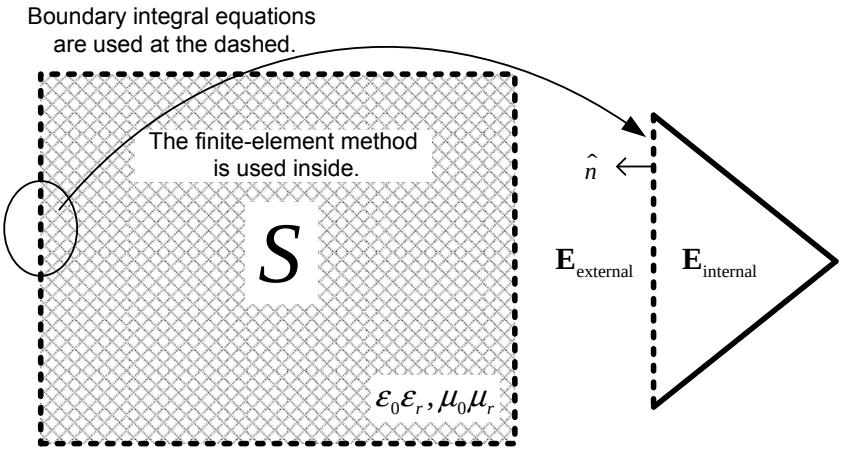

Figure 2.3: Cross section of a rectangular waveguide and one triangular element. The dashed line represents an open boundary which requires $\mathbf{H}_{\text{external}} = \mathbf{H}_{\text{internal}}$.

$$\nabla^2 G(r, r_0) + k_0^2 \varepsilon_r G(r, r_0) = \delta(r - r_0). \tag{2.25}$$

Substituting from (2.24) and (2.25) into (2.23), Green's second identity (2.23) may be written as

$$\int_S \left[H_i(r_0)\nabla^2 G(r, r_0) - G(r, r_0)\nabla^2 H_i(r_0)\right] ds_0 = \oint_C \left[H_i(r_0)\frac{\partial G(r, r_0)}{\partial n} - G(r, r_0)\frac{\partial H_i(r_0)}{\partial n}\right] dr_0. \tag{2.26}$$

Note the left hand side becomes:

$$\int_S \left[H_i(r_0)\left(\delta(r - r_0) - k_0^2 \varepsilon_r G(r, r_0)\right) + G(r, r_0) k_0^2 \varepsilon_r G(r, r_0)\right] ds_0 = H_i(r)$$

and hence

$$H_i(r) = \oint_C \left[H_i(r_0)\frac{\partial G(r, r_0)}{\partial n} - G(r, r_0)\frac{\partial H_i(r_0)}{\partial n}\right] dr_0 \tag{2.27}$$

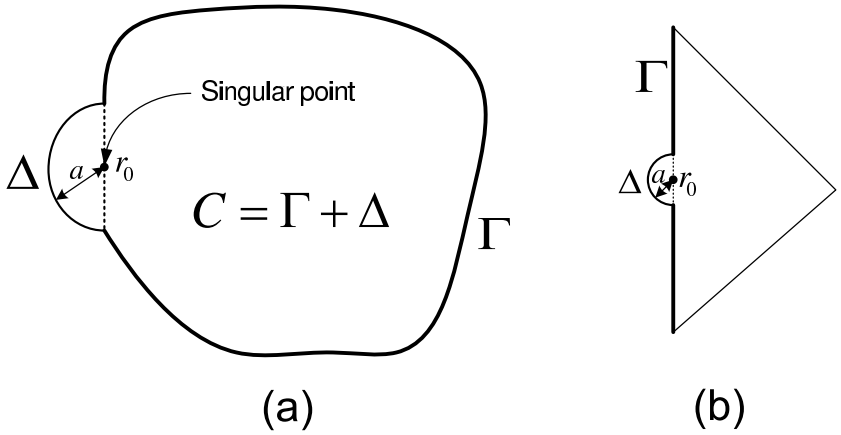

Figure 2.4: Application of the boundary integral equation derived from Green's second identity when the singular point is on the boundary. The total contour C is separated into non-singularity involving contour Γ and singularity involving contour Δ. The radius a is infinitesimally small. (a) General domain with the singular point r_0 and the boundary contour C. (b) One triangular element with the boundary represented by $\Gamma + \Delta$.

where $G(r, r_0) = \frac{1}{2\pi} K_0(\alpha |r - r_0|)$ for the guided mode, $\alpha = \sqrt{\beta^2 - k_0^2}$, K_0 is the modified Bessel function of the second kind. This integration involves a singularity, and the principal value of the integral is used. To remove the singular point r_0 along the contour C, the line integral domain of (2.27) is modified by adding a small half circular area, centered at r_0 with radius a, as illustrated in Fig. 2.4. r_0 is the singular point which should be removed and a is infinitesimally small value. The detail derivation of the principal value integral is expressed through following (2.28)-(2.30).

$$\begin{aligned} H_i(r) &= \oint_C \left[H_i(r_0) \frac{\partial G(r, r_0)}{\partial n} - G(r, r_0) \frac{\partial H_i(r_0)}{\partial n} \right] dr_0 \\ &= \int_\Gamma \left[H_i(r_0) \frac{\partial \left(\frac{1}{2\pi} K_0 \left(\alpha |r - r_0| \right) \right)}{\partial n} - \frac{1}{2\pi} K_0 \left(\alpha |r - r_0| \right) \frac{\partial H_i(r_0)}{\partial n} \right] dr_0 \\ &\quad + \int_\Delta \left[H_i(r_0) \frac{\partial \left(\frac{1}{2\pi} K_0 \left(\alpha |r - r_0| \right) \right)}{\partial n} - \frac{1}{2\pi} K_0 \left(\alpha |r - r_0| \right) \frac{\partial H_i(r_0)}{\partial n} \right] dr_0. \end{aligned} \quad (2.28)$$

Along the singularity involving semi-circular contour Δ, the asymptotic form of $K_0(\alpha|r-r_0|) \approx -\ln(\alpha|r-r_0|)$ can be used because of $|r-r_0| = a \ll 1$. Then,

$$\begin{aligned}
&\int_\Delta \left[H_i(r_0) \frac{\partial\left(\frac{1}{2\pi} K_0(\alpha|r-r_0|)\right)}{\partial n} - \frac{1}{2\pi} K_0(\alpha|r-r_0|) \frac{\partial H_i(r_0)}{\partial n} \right] dr_0 \\
&= \int_\Delta \left[H_i(r_0) \frac{\partial\left(\frac{-\ln(\alpha a)}{2\pi}\right)}{\partial n} + \frac{\ln(\alpha a)}{2\pi} \frac{\partial H_i(r_0)}{\partial n} \right] dr_0 \overset{a\to 0}{=} \left[H_i(r) \frac{1}{2\pi a} + \frac{\ln(\alpha a)}{2\pi} \frac{\partial H_i(r)}{\partial n} \right] \cdot \pi a \\
&= \frac{1}{2} H_i(r) \quad (2.29)
\end{aligned}$$

and

$$\frac{1}{2} H_i(r) = \int_\Gamma \left[H_i(r_0) \frac{\partial\left(\frac{1}{2\pi} K_0(\alpha|r-r_0|)\right)}{\partial n} - \frac{1}{2\pi} K_0(\alpha|r-r_0|) \frac{\partial H_i(r_0)}{\partial n} \right] dr_0. \quad (2.30)$$

In general, the above equation can be written as

$$H_i(r) = \frac{1}{\theta} \oint_C \left[H_i(r_0) \frac{\partial K_0(\alpha|r-r_0|)}{\partial n} - K_0(\alpha|r-r_0|) \frac{\partial H_i(r_0)}{\partial n} \right] dr_0 \quad (2.31)$$

where θ is the exterior angle of the boundary at the singular point r_0 and the principal value of the integral is calculated.

2.4.2 Boundary Conditions

To represent the modal characteristics of open waveguides, the outer boundary condition, which are the continuity of $\mathbf{E}_{tangential}$ and $\mathbf{H}_{tangential}$, needs to be imposed at the surface of the waveguide. The continuity of $\mathbf{H}_{tangential}$ can be obtained directly from the boundary integral equation (2.31). However, the continuity of $\mathbf{E}_{tangential}$ requires the application of

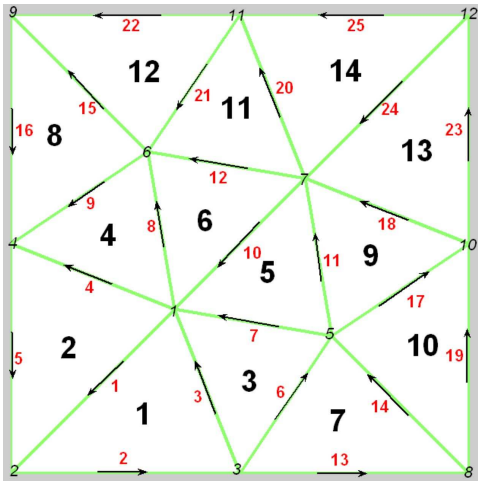

Figure 2.5: Cross section of a rectangular waveguide and it is discretized by 14 triangular elements. In this simple mesh, the number of nodes n and edges e are 12 and 25 respectively. Eight triangular elements, which are element 1,2,7,8,10,12,13, and 14, are involved in boundary conditions. The exterior fields are obtained from the Green's second identity, and the continuity of the tangential E and H-fields are imposed at the surface of the waveguide that is the 8 triangular elements as shown above.

the three components of the vector equation (2.2) and it can be written as

$$\frac{\partial H_z}{\partial y} + j\beta H_y = j\omega\varepsilon E_x \tag{2.32a}$$

$$-j\beta H_x - \frac{\partial H_z}{\partial x} = j\omega\varepsilon E_y \tag{2.32b}$$

$$\frac{\partial H_y}{\partial x} - \frac{\partial H_x}{\partial y} = j\omega\varepsilon E_z. \tag{2.32c}$$

Keeping the transformation of variables $h_x = \beta H_x$, $h_y = \beta H_y$, and $h_z = -jH_z$, (2.32) is reduced to the following

$$j\frac{\partial h_z}{\partial y} + jh_y = j\omega\varepsilon E_x \tag{2.33a}$$

$$-jh_x - j\frac{\partial h_z}{\partial x} = j\omega\varepsilon E_y \tag{2.33b}$$

$$\frac{1}{\beta}\left(\frac{\partial h_y}{\partial x} - \frac{\partial h_x}{\partial y}\right) = j\omega\varepsilon E_z. \tag{2.33c}$$

Now, the boundary conditions require $\mathbf{E}_{tan-ext.} = \mathbf{E}_{tan-int.}$ and $\mathbf{H}_{tan-ext.} = \mathbf{H}_{tan-int.}$ at the surface of the waveguide (see Fig. 2.3). Note that the external field has the form $\mathbf{H}(r)K_0(\alpha\,|r - r_0|)$ to apply the continuity of $\mathbf{E}_{tangential}$. These equations lead to a boundary operator matrix of the form $[B_L]\begin{bmatrix}\mathbf{h}_t\\ h_z\end{bmatrix} = \beta^2\,[B_R]\begin{bmatrix}\mathbf{h}_t\\ h_z\end{bmatrix}$. The problem now remains on how to include these boundary conditions into the the FEM wave equation matrix. In Fig. 2.5, boundary conditions are illustrated with a simple mesh on the cross section of a rectangular waveguide.

2.5 Methods of Solving Eigenvalue Problem and Numerical Results

2.5.1 Iterative Method with Singular Value Decomposition

The following boundary condition matrix is obtained and

$$\left[B_L^{iterative}\right]\begin{bmatrix}\mathbf{h}_t\\ h_z\end{bmatrix} = \beta^2\left[B_R^{iterative}\right]\begin{bmatrix}\mathbf{h}_t\\ h_z\end{bmatrix} \tag{2.34}$$

where $\left[B_L^{iterative}\right]$ and $\left[B_R^{iterative}\right]$ are rectangular matrices. To find accurate solutions for β^2 as the eigenvalue, an initial trial value of β_{trial} obtained from the generalized eigenvalue equation (2.22) is used. Then, the boundary operator equation (2.34) becomes

$$\left[B^{iterative}\right]\begin{bmatrix}\mathbf{h}_t\\ h_z\end{bmatrix} = 0 \tag{2.35}$$

where $\left[B^{iterative}\right] = \left[B_L^{iterative}\right] - \beta_{trial}^2 \left[B_R^{iterative}\right]$. This equation (2.35) is solved using the singular value decomposition (SVD) and the null space obtained from the zero eigenvalue is used to reduce the number of unknowns of the $\begin{bmatrix} \mathbf{h}_t \\ h_z \end{bmatrix}$ vector space.

$$\begin{bmatrix} \mathbf{h}_t \\ h_z \end{bmatrix} = [Z]\,[h_{iterative}]\,. \tag{2.36}$$

Suppose the number of boundary equations is b, the dimension of null space $[Z]$ is at most $(e+n)\times(e+n-b)$ and the size of new eigenvector is $(e+n-b)\times 1$ because the eigenvector $\begin{bmatrix} \mathbf{h}_t \\ h_z \end{bmatrix}$ has a size of $(e+n)\times 1$. Substituting (2.36) into (2.22) and premultiplying both sides by $[Z]^T$ results in [18]

$$\left[L^{iterative}\right][h_{iterative}] = \beta_{new}^2 \left[R^{iterative}\right][h_{iterative}] \tag{2.37}$$

where

$$\left[L^{iterative}\right] = [Z]^T \begin{bmatrix} L_{tt} & 0 \\ 0 & 0 \end{bmatrix} [Z]$$

and

$$\left[R^{iterative}\right] = -\,[Z]^T \begin{bmatrix} R_{tt} & R_{tz} \\ R_{zt} & R_{zz} \end{bmatrix} [Z]\,.$$

Note that β_{new}^2 in this equation is the new trial value to be calculated for this eigenvalue equation and to be used in (2.34). This iterative process continues until the difference of β_{trial} and β_{new} becomes small of the order of 10^{-5} [10]. Fig. 2.6 shows the procedure and it is found that it converges systematically. Near cutoff, $\beta^2 = k_0^2 + \Delta\varepsilon$, $\Delta\varepsilon$ is small. In this situation, the asymptotic expansion of $K_0(\alpha\,|r - r_0|)$ is used in the boundary operator

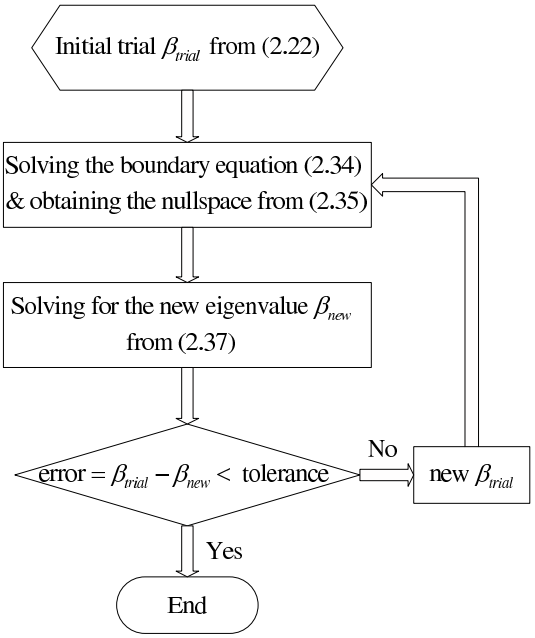

Figure 2.6: Flowchart of the iterative method to find accurate solution. The tolerance should be smaller than 10^{-5}.

equation, and convergence is slow.

The above method was applied to the rectangular dielectric waveguide to find the propagating modes. The results are presented in normalized values:

$$B = \frac{\beta^2 - n_2^2 k_0^2}{\left(n_1^2 - n_2^2\right) k_0^2} = \frac{\beta^2 - \varepsilon_2 k_0^2}{\left(\varepsilon_1 - \varepsilon_2\right) k_0^2}, \quad V = \frac{k_0 W \sqrt{n_1^2 - n_2^2}}{\pi} = \frac{k_0 W \sqrt{\varepsilon_1 - \varepsilon_2}}{\pi}$$

where B is the normalized propagation constant and V is the normalized frequency, n_1 the index in the interior of the guide and n_2 is the external region which is usually free space. Fig. 3 shows the dispersion characteristics for the case $W = L$ and relative permittivity $\varepsilon_r \left(= \frac{n_1^2}{n_2^2}\right) = 1.01$. Good agreement is obtained with the results of Goell [3], which are obtained by the expansion of the electromagnetic fields in terms of a series of circular harmonics. Note that the results of [2] show a cutoff when β approaches $k_0 n_2$ for the

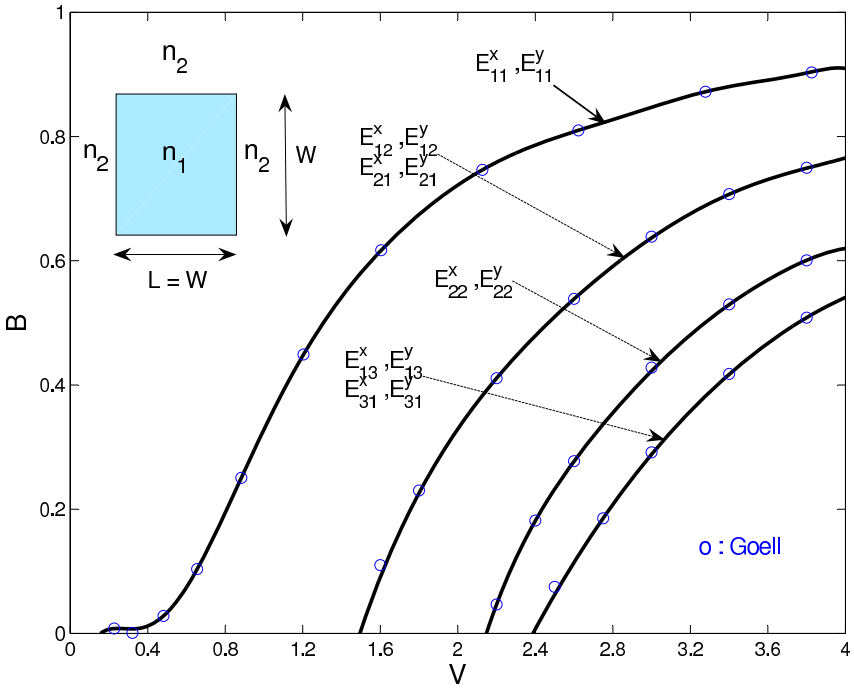

Figure 2.7: Dispersion curves of the first four nondegenerate modes of a rectangular waveguide. The dots are Goell's computer solutions of the boundary value problem. ($W = L$, $n_1^2 = 1.01\varepsilon_0$, $n_2^2 = \varepsilon_0$).

fundamental mode. Goell [3] shows that this mode should have zero cutoff, which is similar to the HE_{11} for the the step index fiber. The results obtained by this method shown in Fig. 2.7 confirm the zero cutoff of the lowest order mode. This singular value decomposition with iteration method [10] has provided the accurate solutions but requires the iterations to obtain the final solutions.

2.5.2 Penalty Function Method

Since both FEM and BIE have the final matrices of the form $Ax = \lambda Bx$, the penalty function method is used [19] [20] [21]. The major advantage of the penalty method technique is that after the penalty factor is specified for each mode, the propagating characteristics are obtained without iterations.

Equations of (2.22) may be simplified by eliminating $[h_z]$ thus:

$$[h_z] = -\left[R_{zz}\right]^{-1}\left[R_{zt}\right]\left[\mathbf{h}_t\right]. \tag{2.38}$$

Substituting (2.38) into the first set of (2.22), a reduced eigenvalue equation in terms of the transverse eigenvectors is obtained [15].

$$[L_{tt}][\mathbf{h}_t] = \beta^2[R_{tt}^{'}][\mathbf{h}_t] \tag{2.39}$$

where $[R_{tt}^{'}] = [R_{tz}][R_{zz}]^{-1}[R_{zt}] - [R_{tt}]$.

To utilize the penalty function method, the continuities of $\mathbf{H}_t$ and E_z are imposed at the surface of the waveguide. Therefore, these boundary conditions results in with the only transverse components

$$\left[B_L^{penalty}\right]\left[\mathbf{h}_t\right] = \beta^2\left[B_R^{penalty}\right]\left[\mathbf{h}_t\right] \tag{2.40}$$

where $\left[B_L^{penalty}\right]$ and $\left[B_R^{penalty}\right]$ are the nonfull rank matrices. For maintaining the identical matrices of the form like (2.39), the near zero expansion of $K_0(\alpha\,|r - r_0|)$ is used in the boundary operator equation (2.40), and finer discretization is required at the boundary. To find the solutions that satisfy both equations (2.39) and (2.40), (2.39) is added to equation

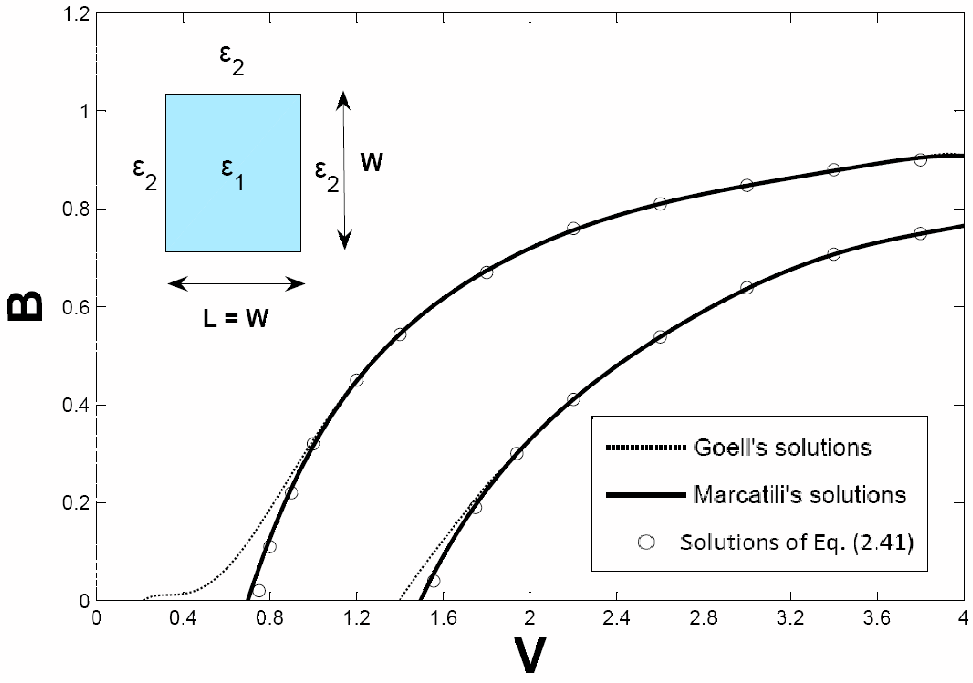

Figure 2.8: Dispersion characteristic of the first two modes of a rectangular waveguide ($W = L$, $\varepsilon_1 = 1.01\varepsilon_0$, $\varepsilon_2 = \varepsilon_0$). The penalty factor of 0.5-0.55 and 0.3-0.4 are used for the fundamental and second mode respectively. The dashed curves represent Geoll's computer solutions, the solid curves are Marcatili's approximate results, the dots are obtained from the penalty function method.

(2.40) with a penalty factor p [19] [20] [21]. Finally, a new generalized eigenvalue equation is obtained with $0 \leq p \leq 1$:

$$\left[p \cdot B_L^{penalty} + L_{tt}\right] [\mathbf{h}_t] = \beta^2 \left[p \cdot B_R^{penalty} + R'_{tt}\right] [\mathbf{h}_t] \,. \tag{2.41}$$

Solution of this equation obtains the propagation constant β^2 as the eigenvalue for a given value of k_0 which is $2\pi/\lambda$, where λ is the free space wavelength. To determine the accuracy of this method, the rectangular dielectric waveguide which is lossless and invariant in the z-direction was analyzed to obtain the dispersion characteristics of the first two modes. The

results are also presented in the normalized form, with the normalized value B and V. The penalty factors of 0.5-0.55 and 0.3-0.4 were used for the first and second mode respectively. The values of the penalty factor was determined by calculating the eigenvalues with the penalty factor ranging from 0 to 1 with steps of 0.1 for a fixed value of k_0 (or λ). Once the value of p is determined, the entire dispersion curve is calculated for different values of V.

Fig. 2.8 shows good agreement with the results of Marcatili [2], which are approximate solutions of the waveguide problem. Near the cutoff frequency for each mode, the agreement with Goell [3] is poorer. For the present case, $W = L$, the permittivity ratio $\varepsilon_r \left(= \frac{\varepsilon_1}{\varepsilon_2}\right) = 1.01$, 930 triangular elements, and 506 nodes were used.

Compared to the iterative method with SVD, no iterations are required once the value of p is determined and smaller matrices are calculated for the generalized eigenvalue problem. However, the accuracy of this method is poorer when propagating modes are investigated near cutoff frequency since few continuity conditions of the field are imposed at the boundary [11].

2.5.3 Pseudoinverse Method

The iterative method with SVD and the penalty function method have been discussed above. These approaches have the advantages of eliminating nonphysical solutions by using edge elements and minimizing the domain needs to be discretized by imposing boundaries at the surface of waveguides. However, both methods have the same limitation that not all the modes are obtained for a given frequency because for the first method is iterative and the second, the mode solution is dependent on the penalty factor. To alleviate these limitations, a psedoinverse method with a penalty factor is proposed in this section.

The continuities of $\mathbf{H}_{tangential}$ and $\mathbf{E}_{tangential}$ lead the boundary condition matrix

$$\left[B_L^{pseudoinverse}\right]\begin{bmatrix}\mathbf{h}_t\\ h_z\end{bmatrix} = \beta^2\left[B_R^{pseudoinverse}\right]\begin{bmatrix}\mathbf{h}_t\\ h_z\end{bmatrix} \tag{2.42}$$

where $\left[B_L^{pseudoinverse}\right]$ and $\left[B_R^{pseudoinverse}\right]$ are rectangular matrices and have the order of $b \times (e+n)$ and b is the number of boundary conditions. Similarly to the earlier penalty function method, the asymptotic form $K_0(\alpha|r-r_0|) \simeq -\ln(\alpha|r-r_0|)$ for $\alpha|r-r_0| \ll 1$ is used to have the identical matrix form of the equation (2.22). Instead of adding the boundary operator equation (2.42) to the generalized eigenvalue matrix equation (2.22), (2.42) is concatenated to the the matrix of the equation (2.22) with a penalty factor to obtain

$$\begin{bmatrix}L_{tt} & 0\\ 0 & 0\\ p\cdot B_L^{pseudoinverse} & \end{bmatrix}\begin{bmatrix}\mathbf{h}_t\\ h_z\end{bmatrix} = \beta^2\begin{bmatrix}-R_{tt} & -R_{tz}\\ -R_{zt} & -R_{zz}\\ p\cdot B_R^{pseudoinverse} & \end{bmatrix}\begin{bmatrix}\mathbf{h}_t\\ h_z\end{bmatrix}. \tag{2.43}$$

To solve this eigenvalue problem ((2.43)), the generalized inverse or called pseudoinverse is used to rearrange it as,

$$\left([A]-\beta^2[I]\right)\begin{bmatrix}\mathbf{h}_t\\ h_z\end{bmatrix} = 0 \tag{2.44}$$

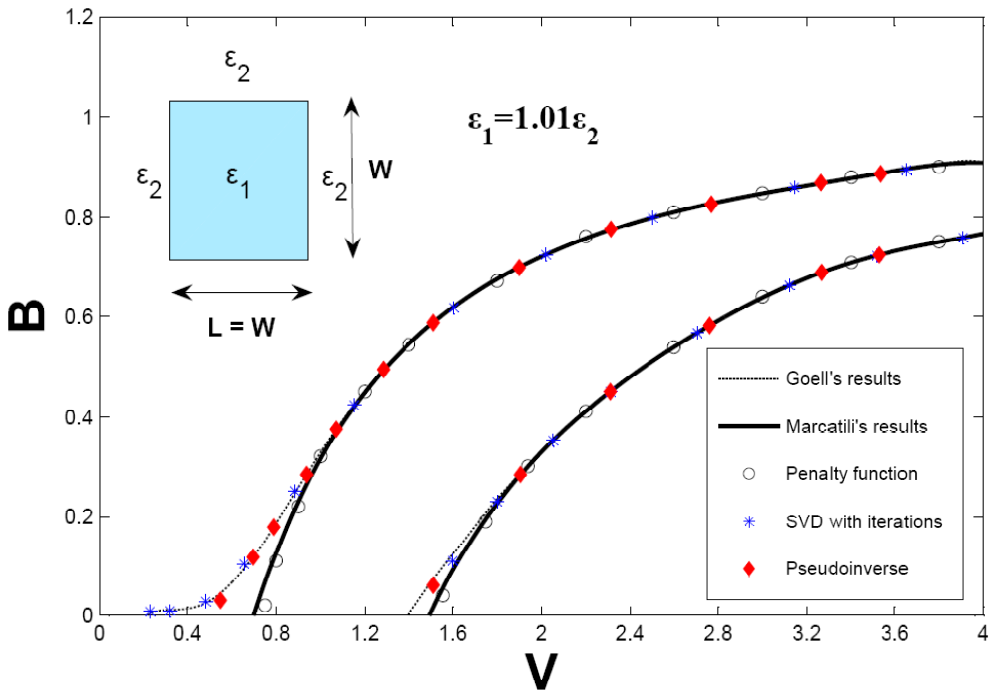

Figure 2.9: Dispersion characteristic of the first two modes of a square waveguide ($W = L$, $\varepsilon_1 = 1.01\varepsilon_0$, $\varepsilon_2 = \varepsilon_0$). Note that solutions of each modes are obtained simultaneously at the operating frequency by using Pseudoinverse method with a penalty factor. The penalty factors of 0.5-0.6 were used for all the simulations.

where

$$[A]_{(e+n)\times(e+n)} = \begin{bmatrix} -R_{tt} & -R_{tz} \\ -R_{zt} & -R_{zz} \\ p \cdot B_R^{pseudoinverse} \end{bmatrix}^{-1} \begin{bmatrix} L_{tt} & 0 \\ 0 & 0 \\ p \cdot B_L^{pseudoinverse} \end{bmatrix}. \tag{2.45}$$

Note that the pseudoinverse is computed using the singular value decomposition technique. This eigenvalue matrix equation is solved to obtain values of β^2 with the penalty factor raging from 0 to 1. The penalty factor of 0 eliminates the outer boundary conditions while the penalty factor of 1 fully includes it. To compare the results with pre-

	Procedure	Size of the final matrix	Advantage	Disadvantage
Iterative method With SVD	Nullspace with iterations	Less than (e+n)×(e+n)	Accurate and zero cutoff of the lowest mode.	Iterations are required.
Penalty function method	Adding matrices with a penalty factor	(e)×(e)	The size of matrices is reduced	Solutions near cutoff are poorer.
Pseudoinverse with a penalty factor	Pseudoinverse with a penalty factor	(e+n)×(e+n)	Accurate and simultaneous solutions are achieved.	Still depends on the penalty factor.

Table 2.1: Comparisons of three different methods

viously published papers, the following parameters were used: the permittivity ratio was $\varepsilon_r \left(= \frac{\varepsilon_1}{\varepsilon_2}\right) = 1.01$, and the cross section was square with $L = W$. In the present finite element calculation, 930 triangular elements were used, and these have 1435 edges and 506 nodes. As shown in Fig. 2.9, the results of this approach are compared with those of Goell [3] and Marcatilli [2] and show good agreement. To determine the penalty factor, solving equation (2.45) while the penalty factor between 0 to 1 by the steps of 0.1 after the normalization of equation (2.43). The penalty factors of 0.5-0.6 were used for all the simulations. The difference of choosing the penalty factor is that the previous method [11] requires a different penalty factor for a particular mode whereas the proposed method provides at least the first two modes with the same penalty factor. This pseudoinverse method with a penalty factor obtains solutions of many modes simultaneously for a fixed value of V, but only two of these solutions are displayed in this figure. In addition, near the cutoff frequency for each mode, the agreement with Goell is better than the penalty function method [11] because continuities of all the transverse and longitudinal fields have been imposed. Since most of the computer run time depends on solving the eigenvalue equation this pseudoinverse method is faster than the iterative method with SVD which requires the

iterative procedure. The more comparisons are summarized in Table 2.1.

Chapter 3

Electromagnetic Scattering by Dielectric Objects

3.1 Introduction

Many approaches have been developed to analyze electromagnetic scattering from three dimensional arbitrary shaped objects [15] [16]. In particular, the method of moments has been used for scattering problems due to having the advantage of being conceptually simple. For homogeneous conducting scatterers, the electric or magnetic field integral equation formulation may be used whereas the combined field integral formulation is required for analyzing homogeneous dielectric scatterers. The surface integral equation approach is well suited to the analysis of electromagnetic scattering by arbitrary shaped objects because the scattered fields excited may be expressed in terms of the equivalent currents on the various intefaces [17]. In order to transform the combined integral equation into matrix equations, the surface of objects is covered by a triangular mesh with the Rao-Wilton-Glisson (RWG)

basis functions for the currents [22] [23]. An appropriate singularity extraction technique to compute the singular single and double surface integrals is discussed in detail when RWG basis functions are applied [24] [25] [26].

For the past several years, high dielectric metamaterials, which show both negative permittivity and negative permeability in a specific frequency range, and its applications have been studied [27]–[30]. Therefore, this methods of moments for dielectric objects is useful to determine whether electric and/or magnetic dipoles exist at various resonant frequencies. Also, this method may be applied to scattering problems in high magnetic field resonance systems since high field MRI systems have the shorter wavelengths within the lossy human subjects. In this chapter, numerical results for the case of lossless and lossy dielectric finite circular cylinders and a cubic high dielectric resonator are discussed. The verification of the existence of the magnetic and electric dipole in the cubic high dielectric resonator is determined and should be useful in metamaterial applications [31].

3.2 Formulation and Numerical Method

3.2.1 Electric Field Integral Equation (EFIE)

In this section, electric field integral equations for the surface current induced on conducting scatterers are obtained from boundary conditions. To derive the integral equations, Maxwell's equation (2.1) is used here and the details follow.

Let S denote the surface of an open or closed perfectly conducting scatterer as shown Fig. 3.1. An electric field $\mathbf{E}^i$, defined to be the field due to an impressed source in the absence of the scatterer, is incident on and induces surface currents $\mathbf{J}$ on S. Note that the surface equivalence theorem, which is a more rigorous formulation of Huygen's principle, is

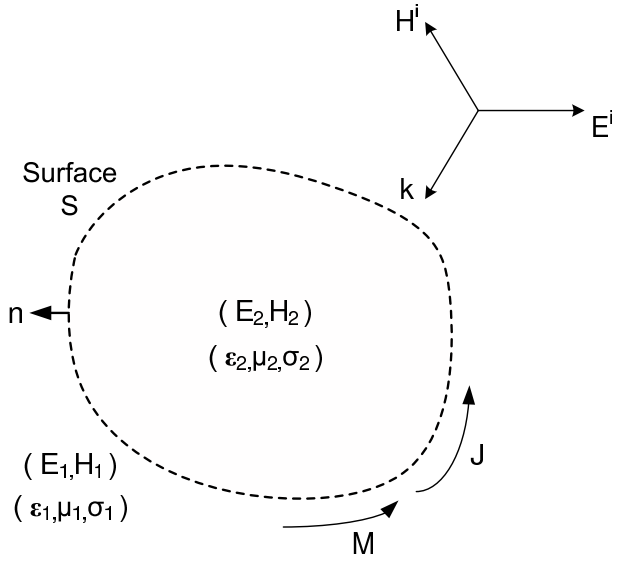

Figure 3.1: Homogeneous dielectric object $(\varepsilon_2, \mu_2, \sigma_2)$ embedded in an homogeneous medium $(\varepsilon_1, \mu_1, \sigma_1)$. $\mathbf{J}$ is the equivalent electric current and $\mathbf{M}$ is the equivalent magnetic current on the surface of the dielectric scatterer. The dashed line represents the surface S of the dielectric object.

basically applied to the integral equation. The scattered (or reflected) electric field $\mathbf{E}^s$ can be derived and computed from the surface current. Thus

$$\nabla \times \mathbf{E}^s = -j\omega\mu\mathbf{H} = -\frac{\partial \mathbf{B}}{\partial t} = -\frac{\partial}{\partial t}\left(\nabla \times \mathbf{A}\right) = -\nabla \times \frac{\partial \mathbf{A}}{\partial t} \tag{3.1}$$

then,

$$\nabla \times \left(\mathbf{E}^s + \frac{\partial \mathbf{A}}{\partial t}\right) = 0. \tag{3.2}$$

Using the vector identity $\nabla \times \nabla V = 0$ leads

$$\mathbf{E}^s = -\frac{\partial \mathbf{A}}{\partial t} - \nabla V = -j\omega\mathbf{A} - \nabla V \tag{3.3}$$

with the magnetic vector potential defined as

$$\mathbf{A}(r) = \frac{\mu}{4\pi}\int_S \mathbf{J}\frac{e^{-jkR}}{R}dS' \tag{3.4}$$

and the scalar potential as

$$V(r) = \frac{1}{4\pi\varepsilon}\int_S \rho^e\frac{e^{-jkR}}{R}dS'. \tag{3.5}$$

The magnetic vector and scalar potentials satisfy the wave equation, the following steps from the Maxwell's second curl equation are used to derive these. Thus

$$\nabla\times\mathbf{H} = \mathbf{J} + \frac{\partial\mathbf{D}}{\partial t} \tag{3.6a}$$

$$\nabla\times\frac{\mathbf{B}}{\mu} = \frac{1}{\mu}\nabla\times\nabla\times\mathbf{A} = \mathbf{J} + \varepsilon\frac{\partial}{\partial t}\left(-\frac{\partial}{\partial t}\mathbf{A} - \nabla V\right) \tag{3.6b}$$

Applying $\nabla\times\nabla\times\mathbf{A} = \nabla(\nabla\cdot\mathbf{A}) - \nabla^2\mathbf{A}$ to (3,6b), then

$$\nabla(\nabla\cdot\mathbf{A}) - \nabla^2\mathbf{A} = \mu\mathbf{J} - \mu\varepsilon\frac{\partial^2\mathbf{A}}{\partial t^2} - \mu\varepsilon\nabla\frac{\partial V}{\partial t}. \tag{3.7}$$

When Lorenz gauge $\nabla\cdot\mathbf{A} + \mu\varepsilon\frac{\partial V}{\partial t} = 0$ is applied, then

$$\nabla^2\mathbf{A} - \mu\varepsilon\frac{\partial^2\mathbf{A}}{\partial t^2} = -\mu\mathbf{J}. \tag{3.8}$$

For the derivation of the scalar potential, apply the divergence on the both sides in (3.3)

and it becomes

$$\nabla \cdot \mathbf{E} = -\nabla \cdot \frac{\partial \mathbf{A}}{\partial t} - \nabla^2 V = \frac{\rho}{\varepsilon} \tag{3.9}$$

and from the Lorenz gauge:

$$\nabla^2 V - \mu\varepsilon \frac{\partial^2 V}{\partial t^2} = -\frac{\rho}{\varepsilon}. \tag{3.10}$$

The solutions of (3.8) and (3.10) may be represented by

$$\mathbf{A}\,(r) = \frac{\mu}{4\pi} \int_S \mathbf{J} \frac{e^{-jkR}}{R} dS' \tag{3.11}$$

and

$$V\,(r) = \frac{1}{4\pi\varepsilon} \int_S \rho^e \frac{e^{-jkR}}{R} dS' \tag{3.12}$$

where $k = \omega\sqrt{\mu\varepsilon}$, and μ and ε are the permeability and permittivity of the surrounding medium and $R = \left| r - r' \right|$ is the distance between an arbitrary observation point r and a source point r'. The surface charge density ρ^e is related to the surface divergence of $\mathbf{J}$ through the equation of continuity,

$$\nabla_s \cdot \mathbf{J} = -\frac{\partial \rho}{\partial t} = -j\omega\rho^e. \tag{3.13}$$

From the boundary condition $\hat{n} \times \left(\mathbf{E}^i + \mathbf{E}^s \right) = 0$ on the conducting boundary S, obtain-

ing

$$-\mathbf{E}^i_{\tan} = (-j\omega\mathbf{A} - \nabla V)_{\tan}, \quad \text{r on S} \tag{3.14}$$

Equation (3.14), with (3.11)-(3.13), constitutes the so-called electric integral equation (EFIE).

3.2.2 Magnetic Field Integral Equation (MFIE)

The magnetic field integral equation (MFIE) results from the magnetic field boundary conditions on the surface of the scattering object

$$\mathbf{J} = \hat{n} \times \mathbf{H}_{\tan} = \hat{n} \times \left(\mathbf{H}^i + \mathbf{H}^s\right) \tag{3.15}$$

where $\hat{n}$ denotes the normal vector to the surface of the scatterer as shown Fig. 3.1. Once the current density is known or determined, the scattered magnetic field can be obtained using (3.1) and (3.11), or

$$\mathbf{H}^s = \frac{1}{\mu}(\nabla \times \mathbf{A}) = \nabla \times \int_S \mathbf{J}\frac{e^{-jkR}}{4\pi R}dS' \tag{3.16}$$

therefore,

$$\hat{n} \times \mathbf{H}^i = \mathbf{J} - \hat{n} \times \left[\int_S \mathbf{J} \times \nabla' \frac{e^{-jkR}}{4\pi R}dS'\right] \tag{3.17}$$

where S is approached by r from the outside and $\mathbf{J}$ is the equivalent electric current.

Equation (3.17) is referred to as the magnetic field integral equation (MFIE) and this is valid only for closed surfaces.

3.2.3 Combined Field Integral Equation (CFIE)

For the derivation of the combined field integral equations, dual equations for electric ($\mathbf{J}$) and magnetic ($\mathbf{M}$) current sources are required as discussed below [17].

Sections 3.2.1 and 3.2.2 explained the electric and magnetic fields with the magnetic vector potential $\mathbf{A}$ assuming only electric current $\mathbf{J}$ exists. Therefore, electric and magnetic fields are represented as

$$\mathbf{H}_A = \frac{1}{\mu}\left(\nabla \times \mathbf{A}\right), \qquad \mathbf{E}_A = -j\omega\mathbf{A} - \nabla V \tag{3.18}$$

where the subscript A denotes the magnetic vector potential $\mathbf{A}$.

Similar to electric sources ($\mathbf{J} \neq 0,\ \mathbf{M} = 0$) based field equations, magenetic sources ($\mathbf{M} \neq 0,\ \mathbf{J} = 0$) based field equations may be written as

$$\mathbf{E}_F = -\frac{1}{\varepsilon}\left(\nabla \times \mathbf{F}\right), \qquad \mathbf{H}_F = -j\omega\mathbf{F} - \nabla U \tag{3.19}$$

with the electric vector potential $\mathbf{F}$ defined as

$$\mathbf{F} = \frac{\varepsilon}{4\pi}\int_S \mathbf{M}\frac{e^{-jkR}}{R}dS' \tag{3.20}$$

and the scalar potential as

$$U = \frac{1}{4\pi\mu}\int_S \rho^m \frac{e^{-jkR}}{R}dS' \tag{3.21}$$

where $\rho^m = -\frac{1}{j\omega}\left[\nabla'_S \cdot \mathbf{M}\right]$ and $\mathbf{M} = \mathbf{E} \times \hat{n}$. Note that the subscript F indicates the fields due to electric vector potential $\mathbf{F}$. Then, referring to the combination of electric and

magnetic sources based formulations and the electromagnetic equivalent principle, scattered electric and magnetic fields in regions 1 and 2 are given by

$$\mathbf{E}_1^s(r) = -j\omega\mathbf{A}_1(r) - \nabla V_1(r) - \frac{1}{\varepsilon_1^{'}}\nabla\times\mathbf{F}_1(r) \tag{3.22a}$$

$$\mathbf{H}_1^s(r) = -j\omega\mathbf{F}_1(r) - \nabla U_1(r) + \frac{1}{\mu_1}\nabla\times\mathbf{A}_1(r), \tag{3.22b}$$

for r on or outside the surface S

$$\mathbf{E}_2^s(r) = j\omega\mathbf{A}_2(r) + \nabla V_2(r) + \frac{1}{\varepsilon_2^{'}}\nabla\times\mathbf{F}_2(r) \tag{3.23a}$$

$$\mathbf{H}_2^s(r) = j\omega\mathbf{F}_2(r) + \nabla U_2(r) - \frac{1}{\mu_2}\nabla\times\mathbf{A}_2(r), \tag{3.23b}$$

for r on or inside the surface S

where $\varepsilon_i^{'} = \varepsilon_i\left(1 - j\frac{\sigma_i}{\omega\varepsilon_i}\right)$ and no loss due to dielectric damping is considered.

On imposing the boundary conditions that the total tangential component of the electric and magnetic field should be continuous across the boundary surface of the arbitrary dielectric object, finally, the following combined field integral equations (CFIE) may be derived as:

$$\mathbf{E}_{\tan}^i(r) = \left\{ j\omega\left[\mathbf{A}_1(r) + \mathbf{A}_2(r)\right] + \left[\nabla V_1(r) + \nabla V_2(r)\right] + \left[\frac{\nabla\times\mathbf{F}_1(r)}{\varepsilon_1^{'}} + \frac{\nabla\times\mathbf{F}_2(r)}{\varepsilon_2^{'}}\right]\right\}_{\tan} \tag{3.24a}$$

$$\mathbf{H}^i_{\tan}(r) = \left\{ j\omega \left[\mathbf{F}_1(r) + \mathbf{F}_2(r) \right] + \left[\nabla U_1(r) + \nabla U_2(r) \right] - \left[\frac{\nabla \times \mathbf{A}_1(r)}{\varepsilon_1'} + \frac{\nabla \times \mathbf{A}_2(r)}{\varepsilon_2'} \right] \right\}_{\tan} \tag{3.24b}$$

where $\mathbf{E}^i$ and $\mathbf{H}^i$ are the incident electric and magnetic fields in the region 1 and the subscript *tan* means tangential component only. A detailed numerical solution method of the coupled integrodifferential equations (3.24a) and (3.24b) is discussed in the following section based on the method of moments with the vector basis functions.

3.3 Method of Moments

Like the finite element method, the method of moments or the moment method has the advantage of being conceptually simple. While the finite element method is useful in solving differential equations, the method of moments is commonly used in solving the integral equations derived through chapter 3.2.

3.3.1 Development of Basis Functions

In order to transform the integral equations into matrix equations, the closed surface S of dielectric scatterers is covered by a triangular mesh, each triangle is defined by a set of edges, faces, and vertices as shown in Fig. 3.2. Fig. 3.3 shows the triangle pair, T_n^+ and T_n^-, associated with the n^{th} common edge of the triangular patch model of the surface S. Points in T_n^+ are designated by the position vector ρ_n^+ defined with respect to the free vertex of T_n^+, V_n^+. Similarly, points in T_n^- are defined by the position vector ρ_n^- pointing toward the free vertex V_n^- of T_n^-. A vector basis function $\mathbf{f}_n$, called Rao-Wilton-Glisson (RWG)

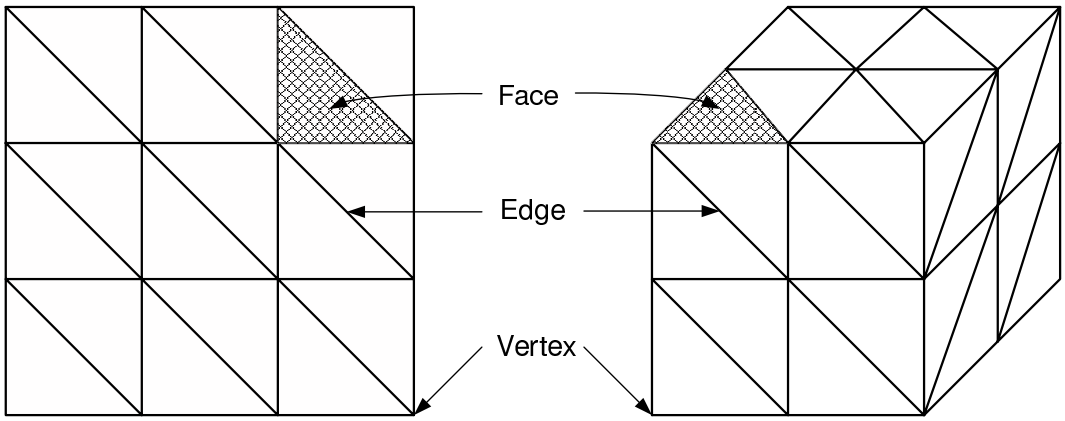

Figure 3.2: The surface modeled by triangular patches. (a) Finite square flat plate. (b) Finite cube dielectric scatterer.

functions, is associated the edge n as [22] [32]

$$\mathbf{f}_n(\mathbf{r}) = \begin{cases} \frac{L_n}{2A_n^+}\rho_n^+ = \frac{L_n}{2A_n^+}\left(\mathbf{r} - \mathbf{V}_\mathbf{n}^+\right), & \mathbf{r} \text{ in } T_n^+ \\ \frac{L_n}{2A_n^-}\rho_n^- = \frac{L_n}{2A_n^-}\left(\mathbf{V}_\mathbf{n}^- - \mathbf{r}\right), & \mathbf{r} \text{ in } T_n^- \\ 0, & otherwise \end{cases} \tag{3.25}$$

where L_n is the length of the common edge n and $A_n^\pm$ are the areas of the pair triangle $T_n^\pm$. From the RWG function properties, the surface divergence of $\mathbf{f}_n$ can be written as

$$\nabla \cdot \mathbf{f}_n(\mathbf{r}) = \begin{cases} \frac{L_n}{A_n^+}, & \mathbf{r} \text{ in } T_n^+ \\ -\frac{L_n}{A_n^-}, & \mathbf{r} \text{ in } T_n^- \\ 0, & otherwise. \end{cases} \tag{3.26}$$

The RWG basis function stated in (3.25) and (3.26) is suitable for representing the equivalent electric current $\mathbf{J}$ and the equivalent magnetic current $\mathbf{M}$ on the triangulated surface S of metal or dielectric scatterers.

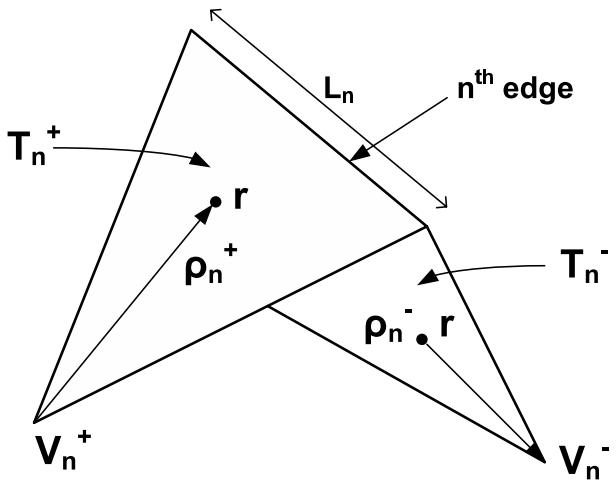

Figure 3.3: Triangle pair associated with the n^{th} edge. Points V_n^+ and V_n^- are the vertices in T_n^+ and T_n^-, respectively.

Referring to the combined field integral equations (CFIE) defined in (3.24), the unknown surface electric and magnetic current, $\mathbf{J}$ and $\mathbf{M}$, are expanded in the RWG basis functions $\mathbf{f}_n$

$$\mathbf{J}(\mathbf{r}) = \sum_{n=1}^{N} J_n \mathbf{f}_n(\mathbf{r}) \tag{3.27a}$$

$$\mathbf{M}(\mathbf{r}) = \sum_{n=1}^{N} M_n \mathbf{f}_n(\mathbf{r}) \tag{3.27b}$$

where N is the total number of edges in the triangulated patch model of the surface S, J_n and M_n are the unknown current coefficients. Once these unknowns are determined, the scattered fields in region 1 and 2 are directly evaluated through (3.22) and (3.23).

3.3.2 Testing Procedure

The next step in the method of moments is to select a testing procedure to find the unknown current coefficients. To retain symmetric inner products, the testing functions are identical

to the basis functions. Thus:

$$\langle \mathbf{f}, \mathbf{g} \rangle \equiv \int_S \mathbf{f} \cdot \mathbf{g} \, dS \tag{3.28}$$

and from (3.24):

$$\left\langle \mathbf{E}^i, \mathbf{f}_m \right\rangle = \left\langle j\omega \left(\mathbf{A}_1 + \mathbf{A}_2 \right), \mathbf{f}_m \right\rangle + \left\langle \left(\nabla V_1 + \nabla V_2 \right), \mathbf{f}_m \right\rangle + \left\langle \left(\frac{\nabla \times \mathbf{F}_1}{\varepsilon_1^{'}} + \frac{\nabla \times \mathbf{F}_2}{\varepsilon_2^{'}} \right), \mathbf{f}_m \right\rangle \tag{3.29a}$$

$$\left\langle \mathbf{H}^i, \mathbf{f}_m \right\rangle = \left\langle j\omega \left(\mathbf{F}_1 + \mathbf{F}_2 \right), \mathbf{f}_m \right\rangle + \left\langle \left(\nabla U_1 + \nabla U_2 \right), \mathbf{f}_m \right\rangle - \left\langle \left(\frac{\nabla \times \mathbf{A}_1}{\varepsilon_1^{'}} + \frac{\nabla \times \mathbf{A}_2}{\varepsilon_2^{'}} \right), \mathbf{f}_m \right\rangle \tag{3.29b}$$

where the subscript m represents an edge formed by two triangles T_m^- and T_m^-. The detail derivation of the terms and in (3.29) can be found in [22] and [32], and the functional from of (3.29) are also derived.

3.3.3 Matrix Equation Derivation

Referring to [22] and [32], the following matrix equation may be obtained for electromagnetic scattering by homogeneous lossy dielectric objects [23]:

$$\begin{bmatrix} [Z_{mn}] & [C_{mn}] \\ -[C_{mn}] & [Y_{mn}] \end{bmatrix} \begin{bmatrix} [J_n] \\ [M_n] \end{bmatrix} = \begin{bmatrix} [V_m] \\ [H_m] \end{bmatrix} \tag{3.30}$$

where elements of the various matrix are given by

$$[Z_{mn}] = L_m \left[\frac{\rho_m^{c+}}{2} \cdot \sum_{i=1}^{2} \mathbf{A}_{i_{mn}}^{+} + \frac{\rho_m^{c-}}{2} \cdot \sum_{i=1}^{2} \mathbf{A}_{i_{mn}}^{-} + \sum_{i=1}^{2} \left(V_{i_{mn}}^{+} - V_{i_{mn}}^{-} \right) \right] \tag{3.31a}$$

where

$$\mathbf{A}_{i_{mn}}^{\pm} = \frac{j\omega\mu_i}{4\pi} \int\limits_{\left(T_n^+ + T_n^-\right)} \mathbf{f}_n\left(r'\right) G_i\left(r_m^{c\pm}, r'\right) dS\left(r'\right) \tag{3.31b}$$

$$V_{i_{mn}}^{\pm} = \frac{1}{4\pi j\omega\varepsilon_i'} \int\limits_{\left(T_n^+ + T_n^-\right)} \left[\nabla \cdot \mathbf{f}_n\left(r'\right)\right] G_i\left(r_m^{c\pm}, r'\right) dS\left(r'\right) \tag{3.31c}$$

and

$$[Y_{mn}] = L_m \left[\frac{\rho_m^{c+}}{2} \cdot \sum_{i=1}^{2} \mathbf{F}_{i_{mn}}^{+} + \frac{\rho_m^{c-}}{2} \cdot \sum_{i=1}^{2} \mathbf{F}_{i_{mn}}^{-} + \sum_{i=1}^{2} \left(U_{i_{mn}}^{+} - U_{i_{mn}}^{-}\right)\right] \tag{3.31d}$$

where

$$\mathbf{F}_{i_{mn}}^{\pm} = \frac{j\omega\varepsilon_i'}{4\pi} \int\limits_{\left(T_n^+ + T_n^-\right)} \mathbf{f}_n\left(r'\right) G_i\left(r_m^{c\pm}, r'\right) dS\left(r'\right) \tag{3.31e}$$

$$U_{i_{mn}}^{\pm} = \frac{1}{4\pi j\omega\mu_i} \int\limits_{\left(T_n^+ + T_n^-\right)} \left[\nabla \cdot \mathbf{f}_n\left(r'\right)\right] G_i\left(r_m^{c\pm}, r'\right) dS\left(r'\right) \tag{3.31f}$$

and

$$G_i\left(r_m^{c\pm}, r'\right) = \frac{e^{-jk_i R^{c\pm}}}{R^{c\pm}}, \quad R^{c\pm} = \left|r_m^{c\pm} - r'\right|. \tag{3.31g}$$

Note that superscript $c\pm$ denotes the centroid of $T_m^{\pm}$ and the matrix elements $[Z_{mn}]$ and $[Y_{mn}]$ are similar except for multiplying constants. Elements of electric and magnetic field excitation:

$$[V_m] = L_m \left[\frac{\rho_m^{c+}}{2} \cdot \mathbf{E}^{i+}\left(r_m^{c+}\right) + \frac{\rho_m^{c-}}{2} \cdot \mathbf{E}^{i-}\left(r_m^{c-}\right)\right] \tag{3.31h}$$

$$[H_m] = L_m \left[\frac{\rho_m^{c+}}{2} \cdot \mathbf{H}^{i+}\left(r_m^{c+}\right) + \frac{\rho_m^{c-}}{2} \cdot \mathbf{H}^{i-}\left(r_m^{c-}\right)\right] \tag{3.31i}$$

Off-diagonal submatrix elements are:

$$[C_{mn}] = \left[\sum_{i=1}^{2} \mathbf{T}_{i_{mn}}^{+} + \sum_{i=1}^{2} \mathbf{T}_{i_{mn}}^{-}\right] \tag{3.32a}$$

where

$$\mathbf{T}_{i_{mn}}^{\pm} = \frac{L_m}{2A_m^{\pm}} \int\limits_{T_m^{\pm}} \rho_m^{\pm}(r) \cdot \left[\frac{1}{4\pi} \int\limits_{(T_n^+ + T_n^-)} \mathbf{f}_n\left(r'\right) \times \nabla' G_i\left(r_m^{\pm}, r'\right) dS\left(r'\right) \right] dS(r) \tag{3.32b}$$

and

$$G_i\left(r_m^{\pm}, r'\right) = \frac{e^{-jk_i R^{\pm}}}{R^{\pm}}, \quad R^{\pm} = \left| r_m^{\pm} - r' \right|. \tag{3.32c}$$

The outer integration with respect to r in (3.32b) has the singularity when $m = n$, and the singular portion of the integrand must be removed to find accurate solution matrices $[J_n]$ and $[M_n]$ in (3.30). To alleviate this singularity problem, the closed form in [24] and the general Gaussian quadrature method are applied to triangular distributions [33]. The specific singular integrations are discussed in the following section.

3.3.4 Treatment of Singular Integral Terms

As mentioned above, an application of the method of moments with RWG functions to solve electromagnetic integral equations requires calculation of single or double integrals with singular kernels. In particular, combined field integral equations for the scattering problem by the dielectric objects has both single and double singular integral equations when observation and source points are on same triangular faces. Equation (3.31b) and (3.31c) take the following simple form having singular term $1/R$ when r^c goes to r'.

$$\int\limits_T G\left(r^c, r'\right) dS\left(r'\right) = \int\limits_T \frac{e^{-jkR^c}}{R^c} dS\left(r'\right) \tag{3.33}$$

where $R^c = \left| r^c - r' \right|$. For simplicity, the barycentric subdivision of an arbitrary triangle as shown in Fig. 3.4 can be used [34]. Any primary triangle from Fig. 3.4 can be divided into

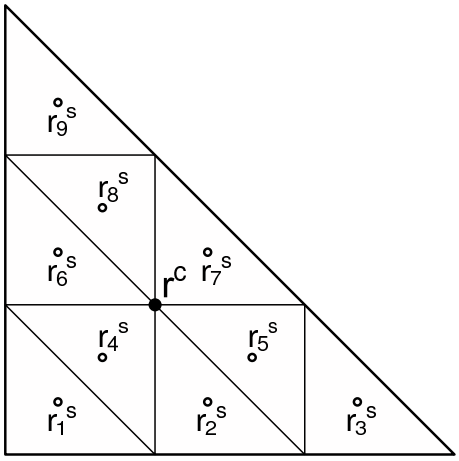

Figure 3.4: Barycentric subdivision of the right angle triangle. The point r^c is a midpoint of the primary triangle T and points r_i^s $(i = 1, 2, \cdots, 9)$ are midpoints of subtriangles.

nine equal small subtriangles, therefore, (3.33) has no singular point and it becomes

$$\int_T \frac{e^{-jkR^c}}{R^c} dS\left(r'\right) = \frac{A_T}{9} \sum_{i=1}^{9} \frac{e^{-jk|r^c - r_i^s|}}{|r^c - r_i^s|} \tag{3.34}$$

where A_T is the area of the primary triangle T and r_i^s are the midpoints of nine subtriangles. This technique generally provides good solutions for the singularity of order $1/R$ on sufficiently regular triangles. In order to get more accurate results, however, more subtriangles are required so the computation time increases.

Another possible solution to (3.33) is to extract the singularity and to calculate the singular term analytically [25] [26]. The Green function G can be evaluated in closed form as:

$$G\left(r^c, r'\right) = \left[G\left(r^c, r'\right) - \frac{1}{R^c} + \frac{k^2}{2} R^c\right] + \frac{1}{R^c} - \frac{k^2}{2} R^c \tag{3.35a}$$

and

$$\int_T \left[G\left(r^c, r'\right) - \frac{1}{R^c} + \frac{k^2}{2} R^c \right] dS\left(r'\right) + \int_T \frac{1}{R^c} dS\left(r'\right) - \frac{k^2}{2} \int_T R^c dS\left(r'\right). \tag{3.35b}$$

Now, the singularities are removed from the first integral in (3.35b) and a standard integration routine on triangles provides accurate results, and no subtriangle is needed. The last two integrals in (3.35b) may be easily integrated in closed form using the references [24] [25] [26].

Next step is to calculate the double singular integral equation (3.32b). This integration has a point singularity of $1/R^2$ which can not be easily evaluated by the barycentric subdivision of an arbitrary triangle and has the difficulty in calculating numerically for the case when T_m and T_n are very close to each other. Therefore, a same idea in the integral of $1/R$ singularity is applied to overcome these problems.

$$\nabla' G\left(r, r'\right) = \nabla' \left(G\left(r, r'\right) - \frac{1}{R} + \frac{k^2}{2} R \right) + \nabla' \frac{1}{R} - \frac{k^2}{2} \nabla' R \tag{3.36}$$

and integrating over triangles T_m with respect to r and T_n with respect to r' takes a simple form:

$$\int_{T_m}(r-v_m)\cdot\left[\int_{T_n}(r'-v_n)\times\nabla' G\left(r,r'\right)dS\left(r'\right)\right]dS\left(r\right) \tag{3.37a}$$

$$=\int_{T_m}(r-v_m)\cdot\left[\int_{T_n}(r'-v_n)\times\left[\nabla'\left(G\left(r,r'\right)-\frac{1}{R}+\frac{k^2}{2}R\right)\right]dS\left(r'\right)\right]dS\left(r\right) \tag{3.37b}$$

$$+\int_{T_m}(r-v_m)\cdot\left[\int_{T_n}(r'-v_n)\times\left(\nabla'\frac{1}{R}\right)dS\left(r'\right)\right]dS\left(r\right) \tag{3.37c}$$

$$+\frac{k^2}{2}\int_{T_m}(r-v_m)\cdot\left[\int_{T_n}(r'-v_n)\times\left(\nabla' R\right)dS\left(r'\right)\right]dS\left(r\right) \tag{3.37d}$$

where $R=\left|r-r'\right|$, v_m and v_n are the free vertices of the triangle T_m and T_n, respectively. Equation (3.37b) has no singularity because its resulting integrand is a smoothly varying function. Equations (3.37c) and (3.37d) must remove the singular portion by using the closed form and numerical integrations. (3.37d) has a point singularity of order $1/R$, therefore, it can be integrated analytically over T_n and the outer integrand can be solved numerically over T_m. The remaining problem is to calculate integrals of $1/R^2$ singularity in (3.37c). To alleviate this difficulty, replacing $(r'-v_n)$ by $(r'-r)+(r-v_m)+(v_m-v_n)$ and separating the normal and surface derivatives result in:

$$\int_{T_m}(r-v_m)\cdot\left[(v_m-v_n)\times\int_{T_n}\left(\nabla'_n\frac{1}{R}+\nabla'_s\frac{1}{R}\right)dS\left(r'\right)\right]dS\left(r\right). \tag{3.38}$$

Referring to [24], the inner integrals of both the normal derivative ∇'_n and the surface derivative ∇'_s of $1/R$ can be calculated in analytical form. For the surface gradient term of

(3.38), the Gauss theorem results a line integral over the boundary of T_n gives [25]

$$\int_{\partial T_n} \left[(v_m - v_n) \times \mathbf{m}\left(r'\right) \right] \cdot \int_{T_m} \frac{(r - v_m)}{R} dS\,(r)\, dl\left(r'\right) \tag{3.39}$$

where ∂T_n represents the boundary of T_n and $\mathbf{m}$ is the outer unit normal of ∂T_n. Now, the inner integral of (3.39) may be evaluated analytically because the logarithmic singularity is removed. Finally, (3.37a) may be solved accurately by integrating all singular terms analytically and applying for numerical integration for non-singular functions. Note that (3.37a) vanishes if T_m and T_n are on the same place.

3.4 Numerical Results

In this section, numerical results are presented for equivalent surface current distributions which give the near and far, even penetrated fields to demonstrate applicability of the above formulations.

3.4.1 Square Flat Plate

Fig. 3.5 shows the surface current distribution along the two principal cuts on a 1.0λ square plate illuminated by a normally incident plate wave. For comparison, the solutions of the conjugate gradient and the fast fourier transform method is given in Fig. 3.5(b) method [35]. The moment method with and without singular extractions is also plotted. As expected, method of moments with closed forms for singular integrations provides more accurate solutions over barycentric subdivision of right angle triangles. Since electric field integration equations for closed conducting scatterers result in single singular integrations of order $1/R$, dividing into nine equal subtriangles discussed in section 3.3.4 generally gives

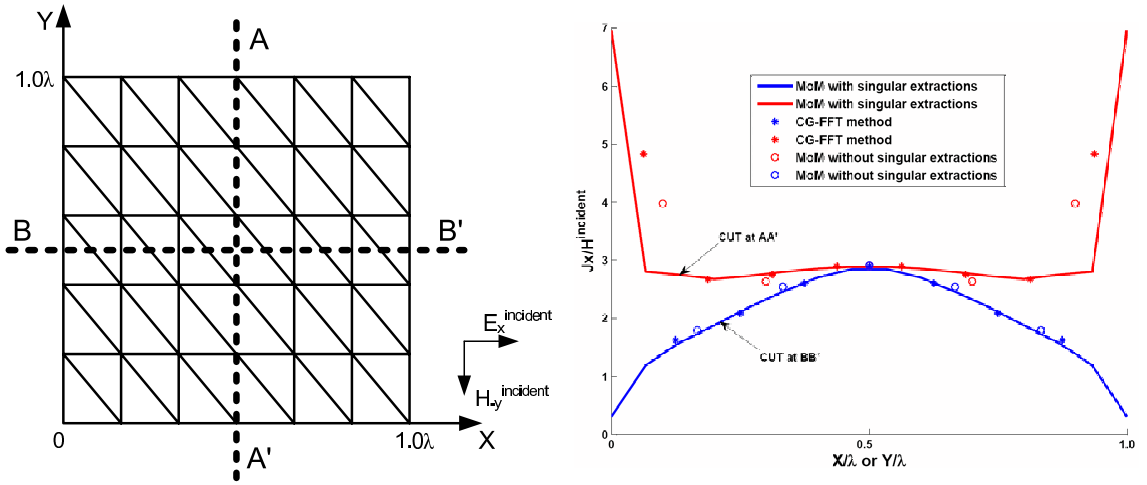

(a) Triangulated patch model

(b) Distribution of dominant of current on 1.0λ square flat plate

Figure 3.5: Triangulated patch model and distribution of the dominant components of surface current across the 1.0λ square flat plate with 60 triangular patches and 79 edge elements.

reasonable solutions as shown in Fig. 3.5(b) (star dots). The solid lines represent solutions of [22] and [32], the circle dots were obtained from the method of moments without singular extractions.

3.4.2 Dielectric Finite Circular Cylinder

To demonstrate applicability of the combined field integral formation, numerical results are presented for the case of a homogeneous dielectric finite circular cylinder located in free space and excited by a plane wave. Fig. 3.6 shows the triangulated patch model on a dielectric finite circular cylinder with 80 triangular patches and 120 edges. The radius and height are 0.1λ and 0.2λ, respectively. For the treatment of double singular integral equations, only 48 edges must be considered for singular extractions when source and observation points are not in the same plane and have common points along those edges.

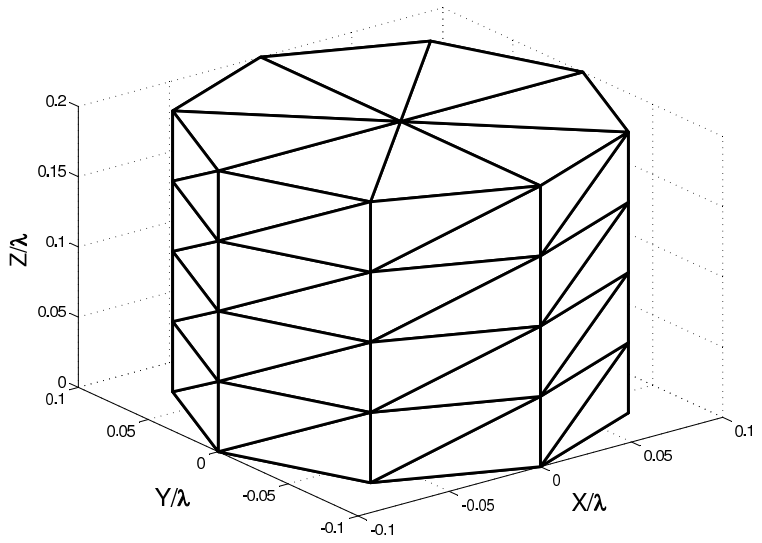

Figure 3.6: Triangulated patch model on a dielectric finite circular cylinder with 80 triangular patches and 120 edge elements. The radius and height are 0.1λ and 0.2λ, respectively.

Fig. 3.7 shows the distribution of equivalent surface electric and magnetic currents for the case of dielectric finite circular cylinder. The relative dielectric constant of the cylinder is $\epsilon_r = 4$ and these results are identical to those in [23].

The next case of higher dielectric constant filled lossy cylinder is plotted in Fig. 3.8. This cylinder has the relative dielectric constant of $\epsilon_r = 58$ and conductivity of $\sigma = 0.6$. These parameters can be used for the human head scattering analysis in the high field magnetic resonance imaging (MRI). For the detail analysis in MRI system, the feeding antenna coil should be modeled by triangular patches instead of the plane wave excitation. The size of cylinder, representing the phantom is also larger, radius of $0.25\lambda_0$ and length of the order of λ_0 where λ_0 is the wavelength in free space.

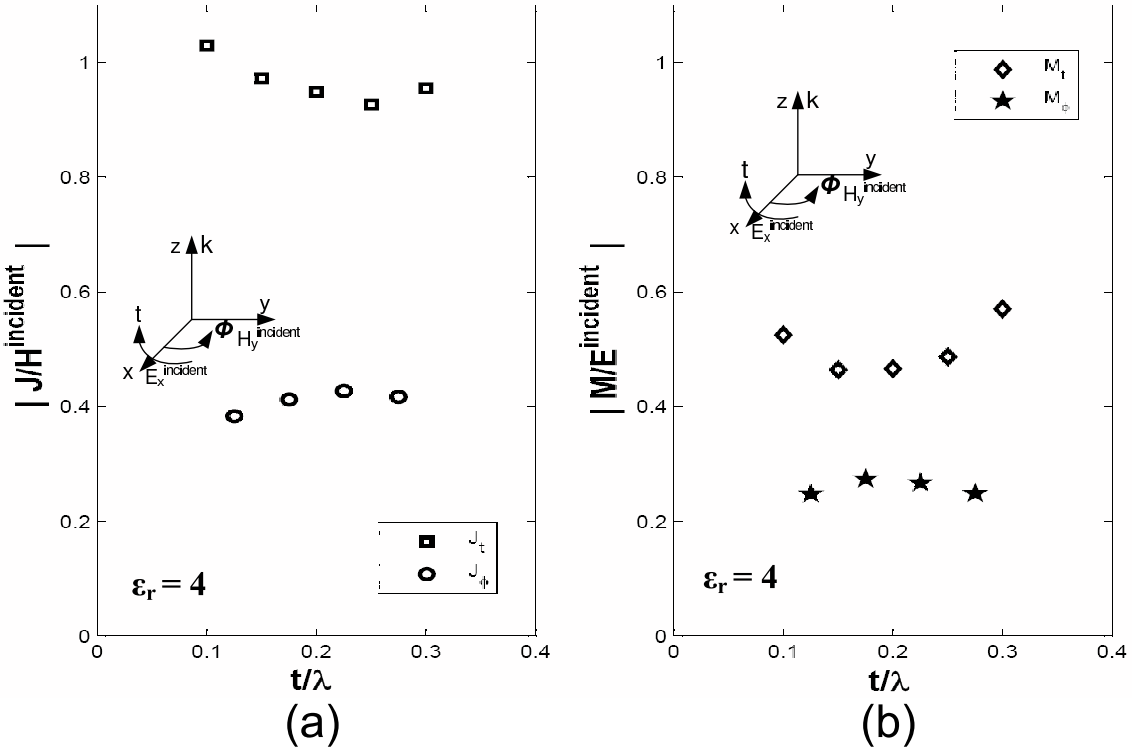

Figure 3.7: Equivalent surface current distribution on a dielectric finite circular cylinder due to a axially incident plane wave. (a) Electric surface current distribution. (b) Magnetic surface current distribution. Note that same results are shown in [23].

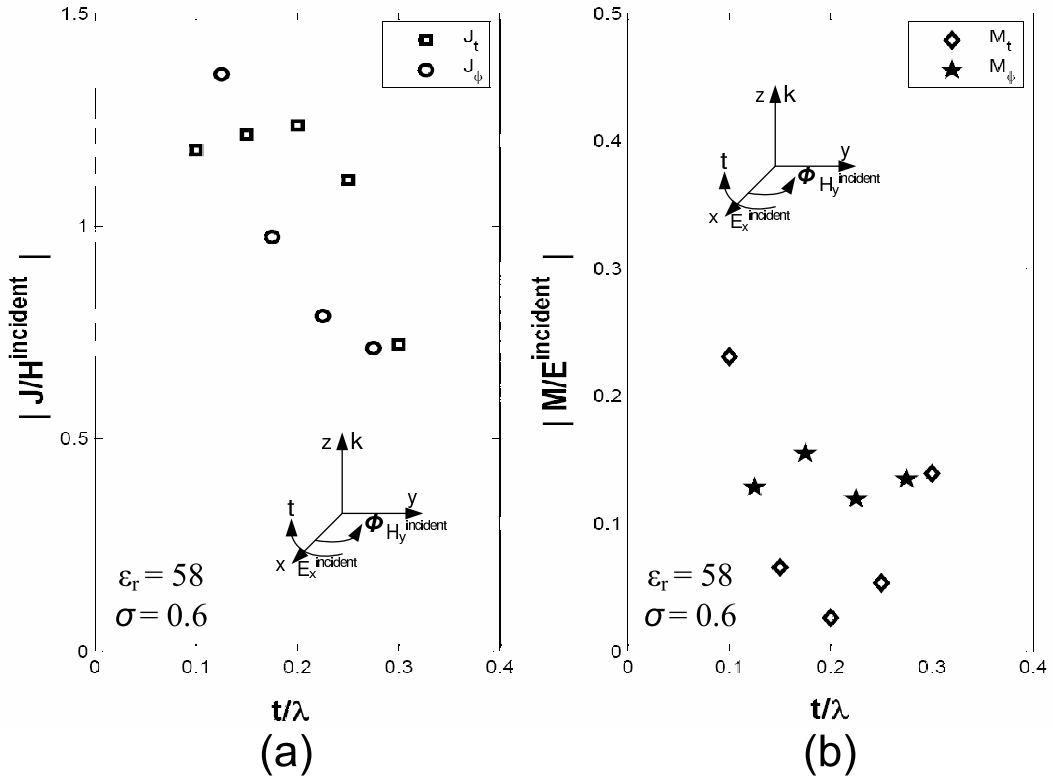

Figure 3.8: Equivalent surface current distribution on a lossy high dielectric finite circular cylinder due to a axially incident plane wave. (a) Electric surface current distribution. (b) Magnetic surface current distribution.

3.4.3 Cubic High Dielectric Resonator Metamaterial

In this subsection, the cubic high dielectric resonator metamaterial is analyzed to examine the penetrated magnetic and electric field distributions. In addition, radiation patterns, $E-$plane and $H-$plane patterns in the far field are plotted in terms of polar coordinates. By definition, the $E-$plane contains the direction of maximum radiation and the electric field vector. Similarly, the $H-$plane contains the direction of maximum radiation and the magnetic field vector. Referring to [30], a rectangular cavity resonator with metal walls has the resonant frequency given by

$$f_{mnp}^{resonant} = \frac{1}{2\sqrt{\mu\varepsilon}}\sqrt{\left(\frac{m}{W}\right)^2 + \left(\frac{n}{H}\right)^2 + \left(\frac{p}{L}\right)^2} \tag{3.40}$$

where m, n, and p represent the integer numbers of half wave variations in the x, y, and z directions, respectively. W, L, and H denote the width, length, height of the rectangular cavity, respectively. Since a high dielectric resonator can be assumed to have magnetic wall boundaries, the first resonant frequency is around 4.838 GHz for the three degenerate modes, TM110, TE011, and TE101 for the 8 mm cubic cavity resonator with $\epsilon_r = 30$ shown in Fig. 3.9. Note that the cubic high dielectric resonator when periodically placed becomes a metamaterial with the negative refractive index characteristic around the resonant frequencies of the cubes, especially for the lowest order mode.

The cross product of $\mathbf{E}$ and $\mathbf{H}$ has the only component in the direction of wave propagation. Moreover the cross product of $\mathbf{E}$ and $\mathbf{H}^*$ (complex conjugate) appears to be a real quantity. This product, divided by 2, is the time-average Poynting vector [36]. The

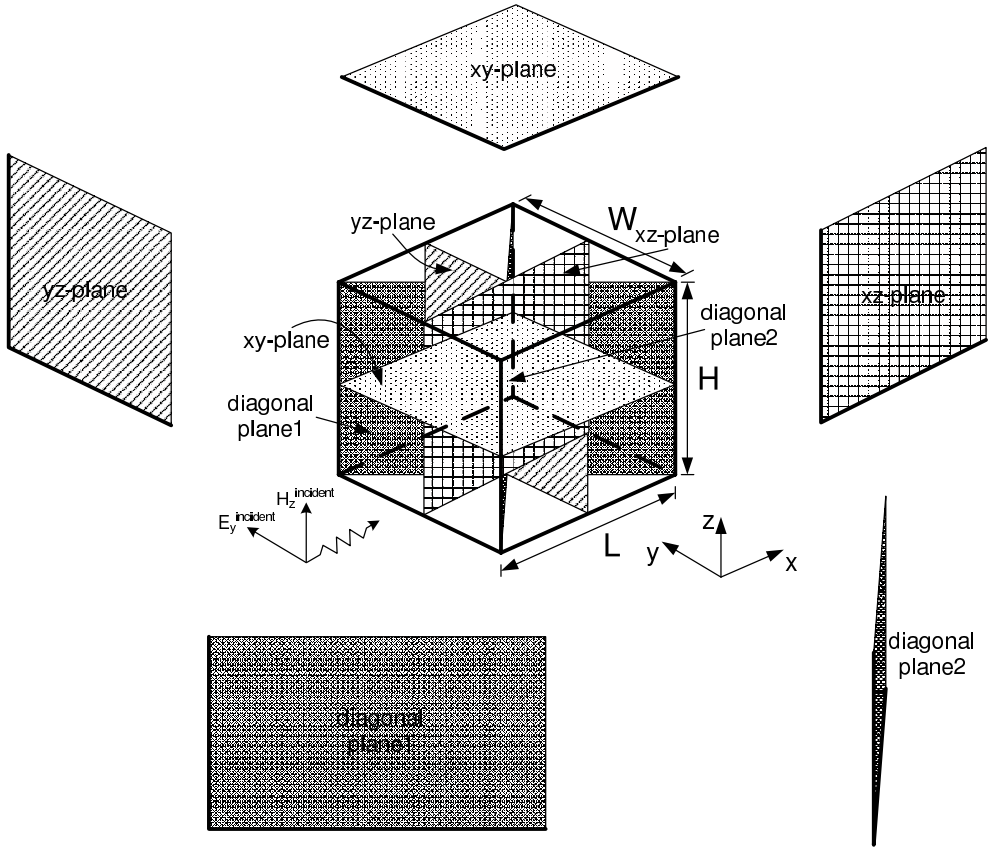

Figure 3.9: Cubic high dielectric resonator metamaterial structure used in the numerical simulation. $W = H = L = 8\ mm$, and $\epsilon_r = 30$. Five different planes are used to obtain magnetic and electric field distributions

Poynting vector a point, $\mathbf{W}$, gives us the average power of the radiated field, per unit area

$$\mathbf{W}(\mathbf{r}) = \frac{1}{2}\mathrm{Re}\left[\mathbf{E}(\mathbf{r}) \times \mathbf{H}^*(\mathbf{r})\right] \tag{3.41}$$

and it has units of W/m^2. Since the radiation density decreases as $1/r^2$ with increasing radius of the observation point, $\mathbf{r}$. It is therefore more convenient to introduce the radiation

intensity, U, which it the radiation density multiplied by r^2, namely

$$U = r^2 W \tag{3.42}$$

where $W = \mathbf{W}(\mathbf{r})\frac{r}{\mathbf{r}}$ and the radiation intensity has units of power (W) per unit solid angle and will theoretically be the same for spheres of different radii surrounding the antenna if the sphere radius is large enough compared to the antenna size and wavelength. For a radiation pattern (or directivity pattern), the antenna directivity is the normalized radiation intensity calculated in dB:

$$D = 10\log_{10}\frac{U}{U_0} \tag{3.43}$$

where the normalization factor U_0 is the total radiated power divided by 4π. In order to calculate the total radiated power, a numerical integration of the flux of radiated energy over a large sphere. In our cases such an integration is not possible, then the radiation pattern is normalized to maximum value of U. Therefore, the radiation patterns have a directivity below 0dB in the direction of minimum radiation. Note that all patterns are calculated when $kr > 10\pi \gg 1$.

Fig. 3.10 shows penetrated magnetic and electric field distributions on five planes for the case of the homogeneous high dielectric cube located in free space and externally excited by a plane wave propagating along the x direction with its electric field $\mathbf{E}^i$ polarized along the y axis. As expected from [30], the magnetic dipole is obtained at the first resonant mode, 5.5 GHz. radiation patterns, $E-$plane and $H-$plane patterns in the far field are plotted in Fig. 3.11 and 3.12, respectively. These patterns confirm characteristics of the dipole.

At the second resonant mode, 7.5 GHz, the high cubic resonator has the electric dipole instead of the magnetic dipole as shown in Fig. 3.13. Since the magnetic fields have

relatively low field strength, there is no effects on radiation patterns, $E-$plane and $H-$plane patterns plotted in Fig. 3.14 and 3.15.

Finally, the cubic dielectric resonator has simultaneously strong electric and magnetic resonance at 8.21 GHz as shown in Fig. 3.16. The maximum magnetic field strength is approximately 0.5, which is more than three times of it at the first resonance. Moreover, The maximum electric field strength is six times higher than maximum electric field strength at the second resonance. These simultaneously strong electric and magnetic fields show characteristics of the quadrupole as shown in Fig. 3.17 and 3.18.

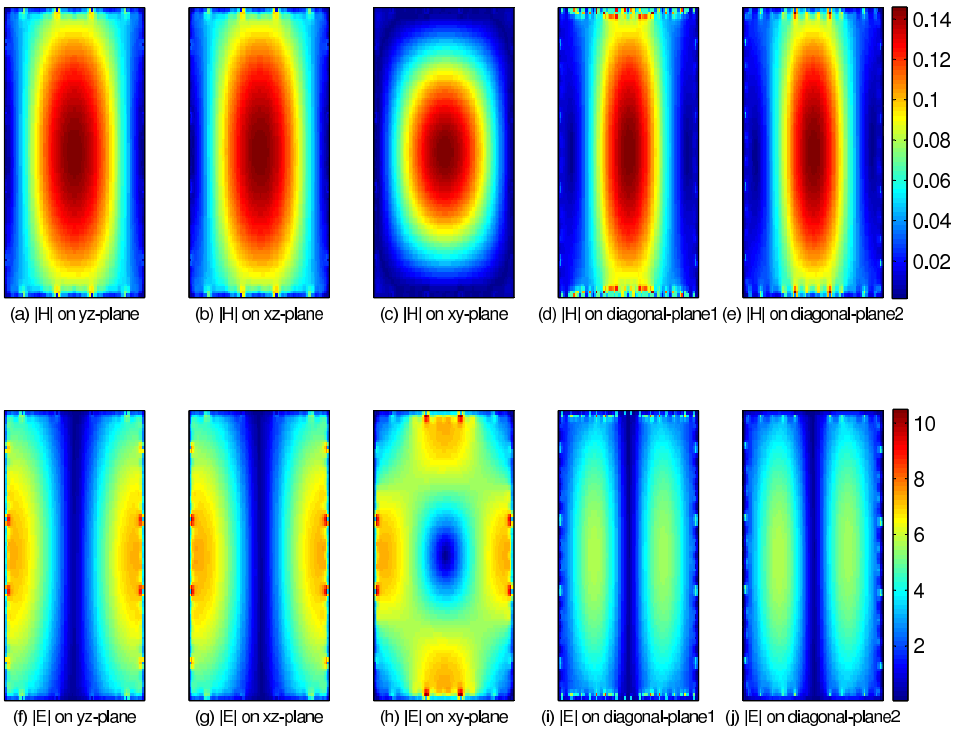

Figure 3.10: Magnetic and electric field distributions of the first resonant mode at 5.5 Ghz. Note that the magnetic dipole is shown due to the resonance.

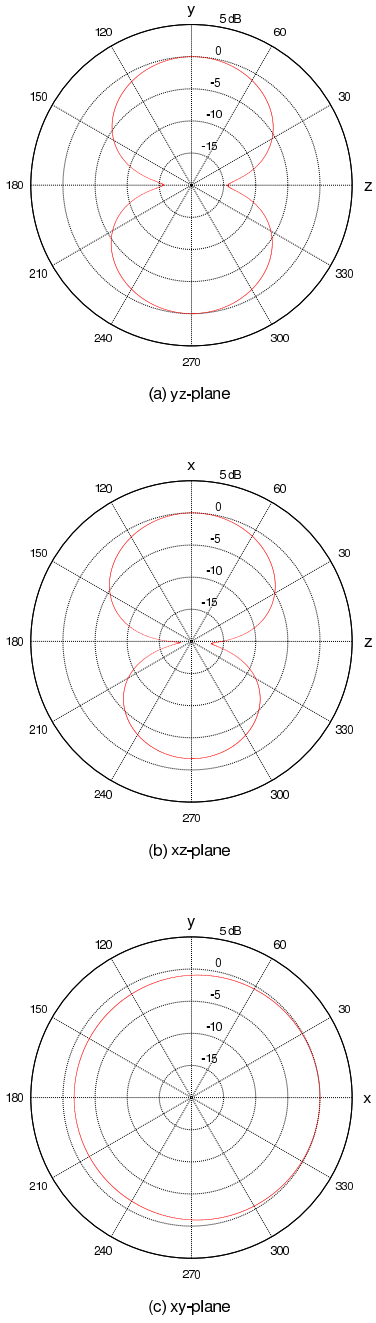

Figure 3.11: Radiation patterns of the high dielectric cube resonator in the yz-, xz-, and xy-planes at 5.5 GHz.

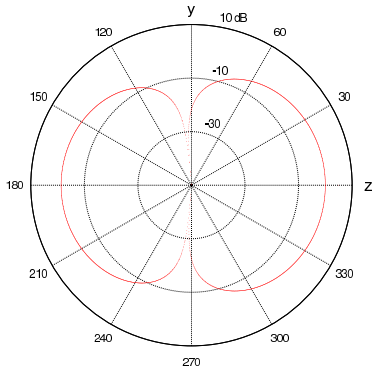

(a) E_θ pattern in the yz-plane

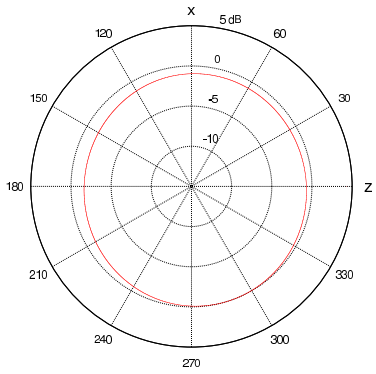

(b) E_θ pattern in the xz-plane

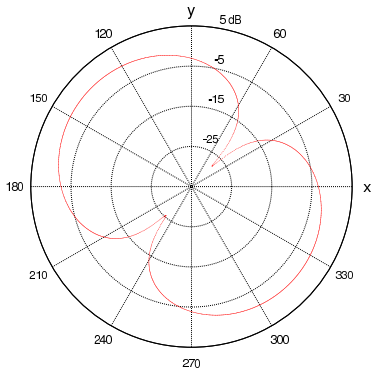

(c) H_ϕ pattern in the xy-plane

Figure 3.12: E_θ patterns and H_ϕ pattern of the high dielectric cube resonator in the yz- and xz-planes, xy-plane, respectively at 5.5 GHz.

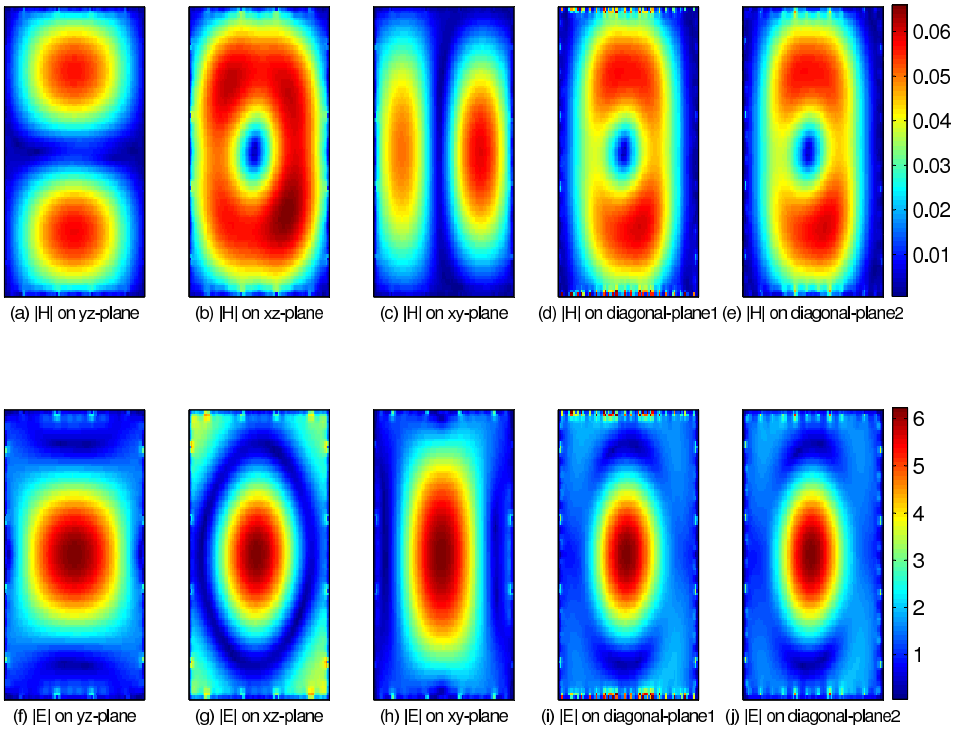

Figure 3.13: Magnetic and electric field distributions at 7.5 GHz. Note that the electric dipole is shown due to the resonance.

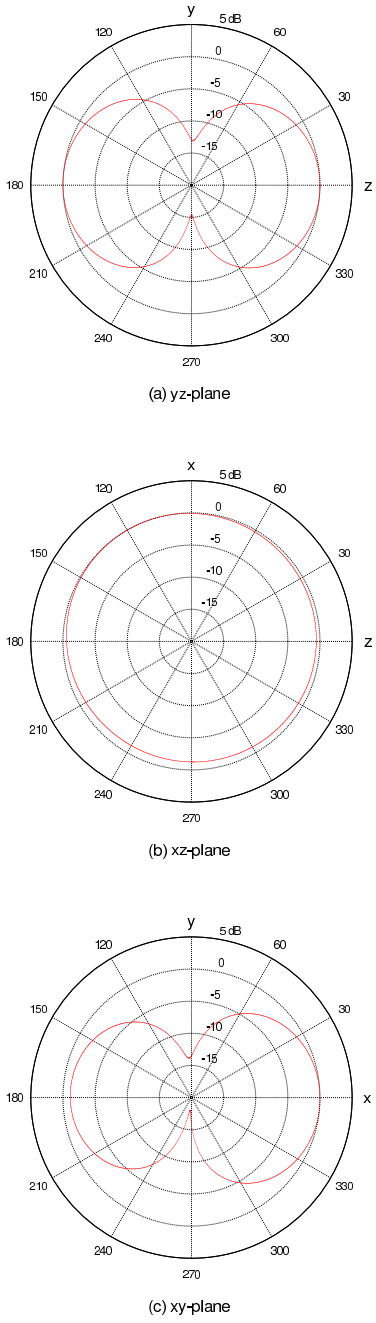

Figure 3.14: Radiation patterns of the high dielectric cube resonator in the yz-, xz-, and xy-planes at 7.5 GHz.

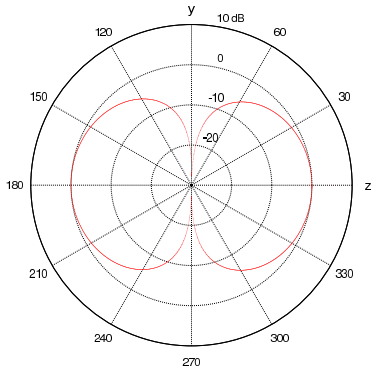

(a) E_θ pattern in the yz-plane

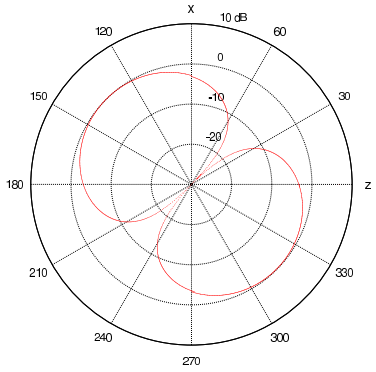

(b) E_θ pattern in the xz-plane

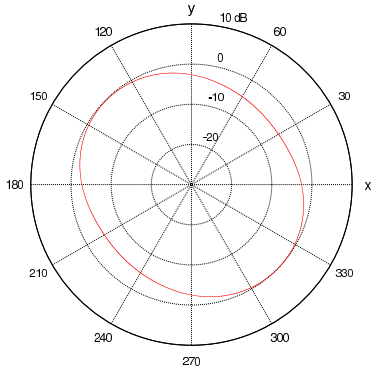

(c) H_ϕ pattern in the xy-plane

Figure 3.15: E_θ patterns and H_ϕ pattern of the high dielectric cube resonator in the yz- and xz-planes, xy-plane, respectively at 7.5 GHz.

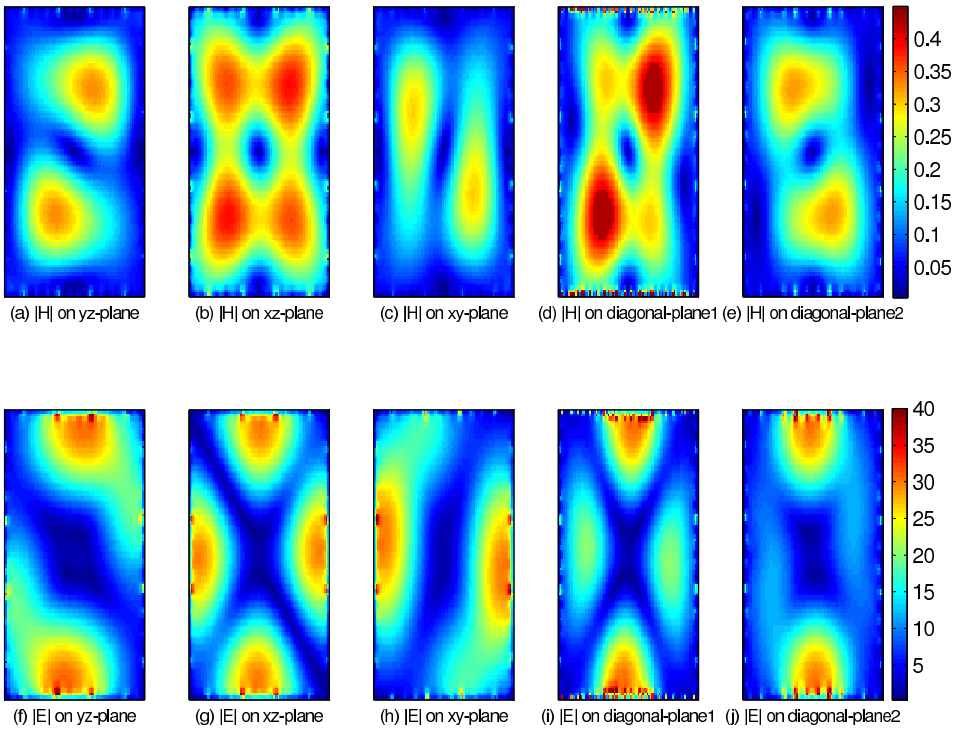

Figure 3.16: Magnetic and electric field distributions at 8.21 GHz. Note that simultaneously strong electric and magnetic resonance are shown at 8.21 GHz

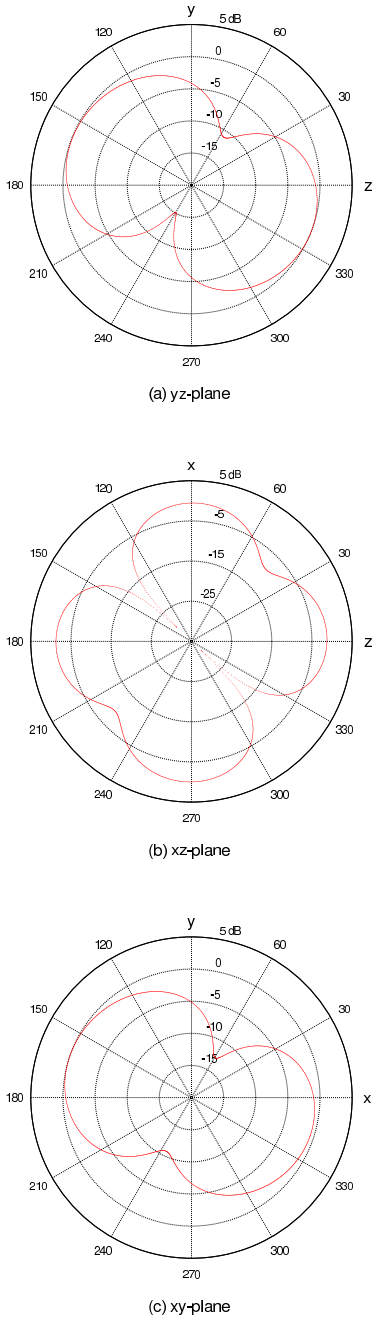

Figure 3.17: Radiation patterns of the high dielectric cube resonator in the yz-, xz-, and xy-planes at 8.21 GHz.

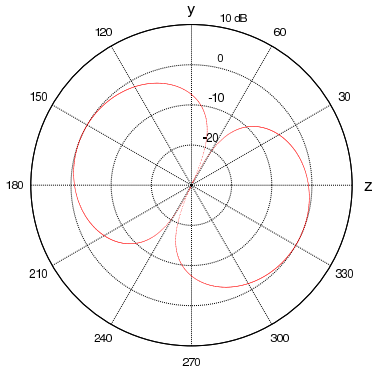

(a) E_θ pattern in the yz-plane

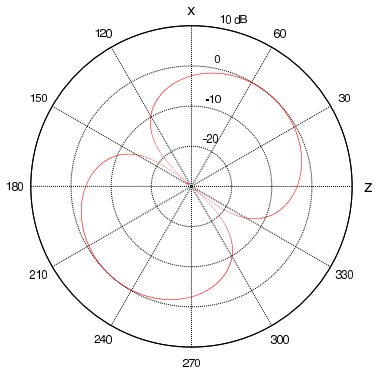

(b) E_θ pattern in the xz-plane

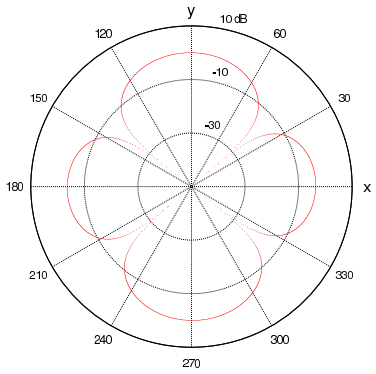

(c) H_ϕ pattern in the xy-plane

Figure 3.18: E_θ patterns and H_ϕ pattern of the high dielectric cube resonator in the yz- and xz-planes, xy-plane, respectively at 8.21 GHz.

Chapter 4

RF B_1 Field Localization in High Magnetic Field Systems

4.1 Introduction

High magnetic field magnetic resonance imaging scanners with B_0 fields of 4T, 7T and 9.4T improve the signal to noise ratios (SNR) [37] [38]. However, the transverse radio frequency magnetic B_1 field non-uniformity also occurs due to the increased RF field frequencies when wavelengths in human anatomy become smaller than its size. Assuming the relative permittivity of 70 ($\varepsilon_r = 70$) in the human head, the wavelength is approximately 9 cm and 12 cm for 9.4T and 7T, respectively. In general, B_1 field inhomogeneity is not significant in low field MR systems and becomes a serious problem as field strength increases.

Since MRI applications require homogeneous B_1^+, which is the circularly-polarized component of the RF B_1 magnetic field, over the object, many approaches have been investigated to minimize B_1^+ non-uniformity [39]–[44]. In particular, multi-channel coils for the

parallel imaging have become important and they provide high local SNR, which can be used for parallel imaging. However, destructive B_1^+ interference patterns also occur when the multi-channel transmission line (transverse electromagnetic (TEM)) coil is used. To control B_1^+ field at high fields, in multiple channel transmission line coils, the control of the amplitude and phase of individual coil elements is required in order to develop the desired B_1^+ field. The choice of the excitation of the coil elements may be determined by convex optimization [45]. Convex optimization is used to provide optimal results rapidly, when the problem is formulated globally. The need to calculate fast solutions is critical to minimize the errors that occur due to patient movement. In addition, convex optimization provides better signal to noise (SNR) ratio when anatomic specific regions are investigated [46] [47]. Although the previous results with convex optimization show these advantages, problems remain, including high field distribution at the edges and non-homogeneity in suppression region.

In this chapter, a better approach is demonstrated with an iterative method, which makes this method useful. Simulation results are compared for 7T and 9.4T systems based on the number of elements. An experiment was performed using an eight channel transmission line coil, and the results are included confirming the theoretical prediction.

4.2 Mathematical Formulation of the Localization Problem

4.2.1 Generating transmit B_1^+ Field

The circularly-polarized component of the RF B_1 magnetic field inside the object is defined as [48]

$$B_1^+ = (B_x + iB_y)/2 \tag{4.1}$$

where $i = \sqrt{-1}$, and B_x and B_y are the complex vectors of x and y directional RF magnetic fields, respectively. There are several numerical methods for calculating this B_1^+ matrix. For instance, finite element method in chapter 2 and moment methods in chapter 3 may be used. Here, B_x and B_y are obtained with the finite difference time domain (FDTD) numerical method by simulating steady-state fields and RF B_1 fields. These calculations are performed at 300 MHz and 400 MHz for the 7T and 9.4T MRI system respectively throughout a head and phantom model in a multi-channel coil.

4.2.2 Convex Optimization

The primary objective of this study is to increase the signal in a specific target region and decrease the signal and noise in the outside region termed the suppression region [46] [47]. Since B_1^+ is proportional to w which is the linear amplitude and phase of the each generated element weight, the positively polarized transmit field with w at each element may be written as $\sum B_1^+ w$ for the total field representation. The following are basic convex formulations which satisfy the initial objective,

$$\begin{aligned} &\textbf{minimize} \quad \max \left| B_{1,s}^+ w \right| \quad s \in \text{Suppresion Region} \\ &\textbf{subject to} \quad B_{1,c}^+ w = 1 \quad c \in \text{Center of Target} \end{aligned} \tag{4.2}$$

where $B_{1,s}^+$ and $B_{1,c}^+$ represent B_1^+ in the suppression region and at the center of the region of interest (ROI), respectively. Equation (4.2) states the constraints for solving for the optimal w while minimizing the maximum value of $B_1^+ w$ in the suppression region by setting the center value of $B_1^+ w$ to unity. From the above formulation, $B_{1,s}^+$ fields are more significant in determining the optimal w since $B_{1,s}^+$ consists of a large number of field points, whereas $B_{1,c}^+$ is the field at one point. Under these constraints, an appropriate selection of $B_{1,s}^+$

is required to obtain the homogeneous suppression region, which can alleviate anomalous contrast. The solution w of (4.2) was calculated by CVX, which is a modeling system for convex programming and, the newest version, SDP3 solver, is used [49]. To find the optimal $B_{1,s}^{+}$, the following iteration algorithm is used in combination with convex formulations.

4.2.3 Iterative Method

Based on the above min-max optimization criterion, the selection of $B_{1,s}^{+}$ is critical to a proper design of w at the given $B_{1,c}^{+}$ because these vector fields are correlated with each other in terms of the solution of w. The homogeneous coefficient H in the suppression region is defined as

$$H = \left(\sum_{i=1}^{n} \left| B_{1,i,s}^{+} w \right| - M(w) \right) / n \tag{4.3}$$

where $M(w)$ is an absolute mean value of $B_{1,s}^{+} w$ and n is the number of pixels in the suppression region. The homogeneous coefficient H, which represents how the homogeneous $B_1^{+} w$ fields are in the suppression region, and the lower H value implies homogeneity. Hence, the basic concept for the iteration algorithm is to minimize H by modifying $B_{1,s}^{+}$.

As shown in Fig. 4.1, the iterations are performed by comparing the new homogeneous coefficient H_{new} of the solution to H_{old} of the previous solution. Since the field maximum at the center of the target region is held to unity, it is reasonable that the neighbor fields at the center are close to unity and they decrease as the distance from the center increases. Accordingly, it is also important to observe this distance when modified $B_{1,s}^{+} w$ is chosen at the different field strength. This decay length depends on the static field strength B_0, and a longer length may be predicted at lower B_0 intuitively. By applying this property to the modification of $B_{1,s}^{+} w$, the relation which produces poor homogeneity between the object

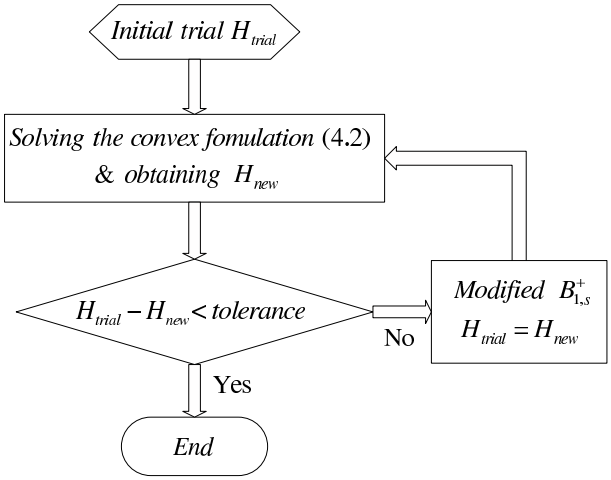

Figure 4.1: In the flow chart of the iteration algorithm, the tolerance is compared to between H_{trial} and H_{new} after the modification of $B_{1,s}^{+}w$ and it can be chosen depending on H_{trial}. The modification is repeated by searching the values close to max $\left|B_{1,s}^{+}w\right|$ near to the target region and excludes those vectors in the next iteration.

and subject function may be eliminated, therefore, a better homogeneity in the suppression region may be obtained. The details are discussed below in the simulation results.

4.3 Simulation Results

To perform simulations of B_1^+ distributions in a human head and phantom model, XFDTD commercial software (Remcom, State College, PA, USA) was used at 300 and 400 MHz in order to reproduce 7T and 9.4T systems, respectively. Since B_x and B_y complex data are generated from one coil element with steady-state analysis for a 16-channel head coil, total B_1^+ can be obtained by duplicating 16 data sets properly. All the B_1^+ field components were exported in an axial plane crossing the center of each model at 120×120 and 90×90 grid points for a human head and phantom model, respectively. When these steady-state values are calculated, each amplitude and phase drive for the coil element is set to unity to

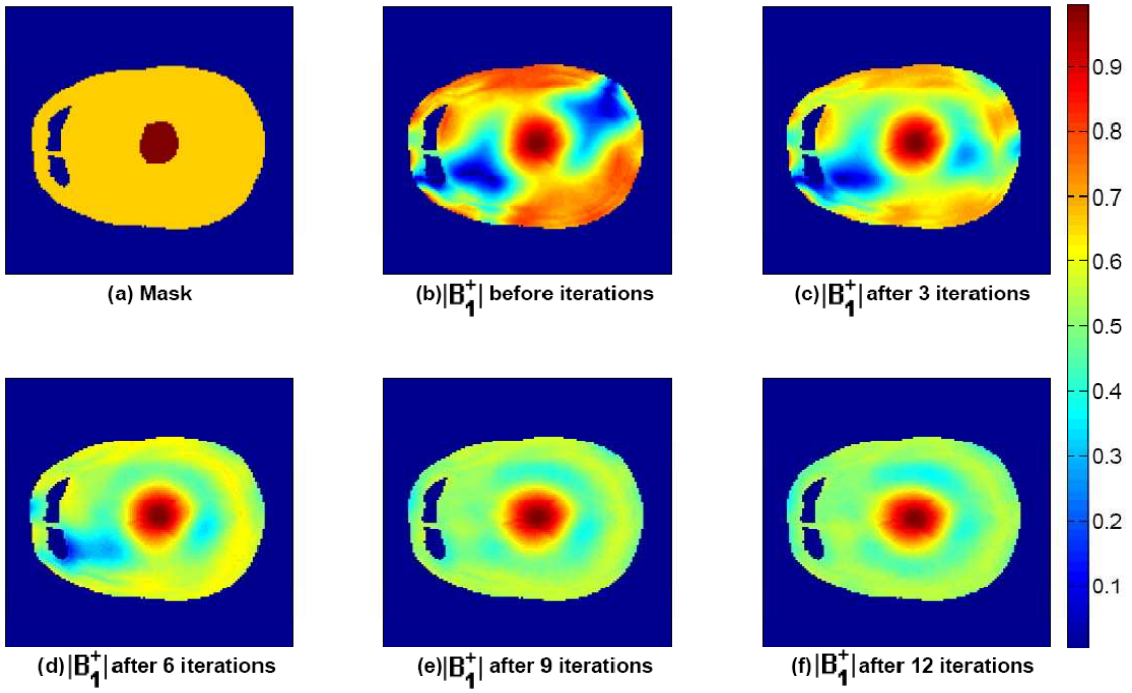

Figure 4.2: Finite Difference Time Domain Human Head Model Results at 9.4T (400MHz) when the 16 channel head coil is used. (a) A head model mask and ROI is at center. (b) $\left|B_1^+\right|$ result with initial convex optimizations. (c)-(f) $\left|B_1^+\right|$ results after applying the iterative method.

measure initial homogeneity before arriving at the amplitude and phase of the optimized excitation.

4.3.1 Human Head Model

The results of the localization on FDTD human data at 9.4T are shown in Fig. 4.2, 4.3, and 4.4. In these figures, the axial slices of the center of human head model provided by XFDTD are used after manipulation with MATLAB. Fig. 4.2 and 4.3 show an improvement of the homogeneity in the suppression region when the target region (dark brown in Fig. 4.2(a)) is at center. As shown in Fig. 4.2(b), this $\left|B_1^+\right|$ distribution comes after solving (4.2) based only on the mask in Fig. 4.2 (a). Although the $\left|B_1^+\right|$ field is desirable in the

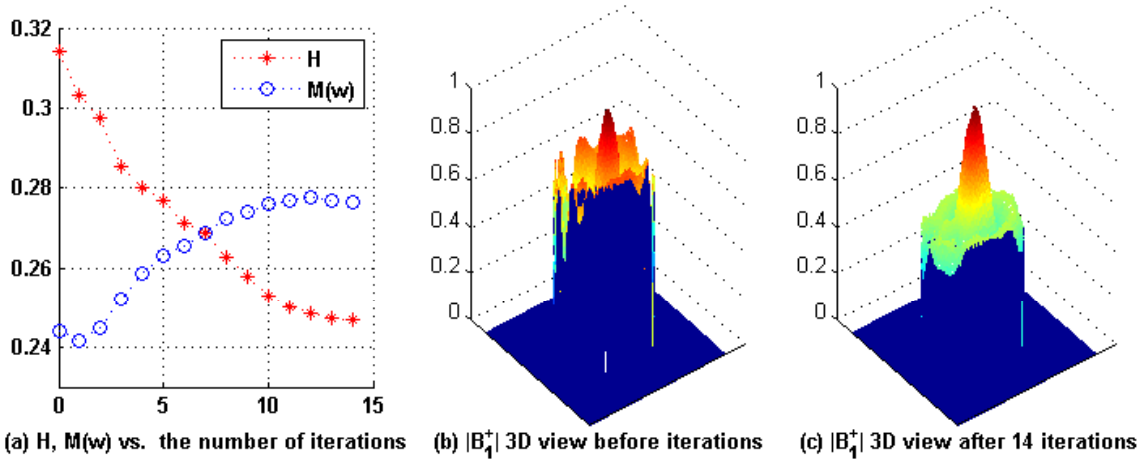

Figure 4.3: (a) The homogeneous coefficient H and the absolute mean value $M(w)$ in the suppression region depending on the number of iterations. (b) $\left|B_1^+\right|$ 3-dimension view with initial convex optimizations (Fig.2 (b)). (c) $\left|B_1^+\right|$ 3-dimension view after 14 iterations and it shows a lot of are $\left|B_1^+\right|$ suppressed, especially at the edge.

target region, it is not large enough to distinguish it from the noise of the whole region due to a poor homogeneity in the suppression region. To avoid this, the modified $B_{1,s}^+$ from new excitation parameters is applied iteratively. As seen in Fig. 4.2(b-f), the homogeneity is improved significantly, whereas $\left|B_1^+\right|$ on the target remains almost constant. In particular, these iterations reduce $\left|B_1^+\right|$ at the edge of the head (Fig. 4.3(b, c)). The iterations of convex optimization are performed until the decrease of the homogeneity coefficient, H, no longer occurs. It also makes the absolute mean value $M(w)$ in the suppression region somewhat larger (Fig. 4.3(a)). When the region of interest moves to the edge of the field of view, the results are shown in Fig. 4.4, and the $\left|B_1^+\right|$ results before and after iterations of convex optimization are shown in Fig. 4.4(c) and 4.4(f). In addition, weights are shown in Fig. 4.4(d) and the distribution of these weights after iterations is more uniform. The homogeneity in the suppression region is improved, but not as much as when the region of interest was centered because of the lack of symmetry. Since weights w are designed for the

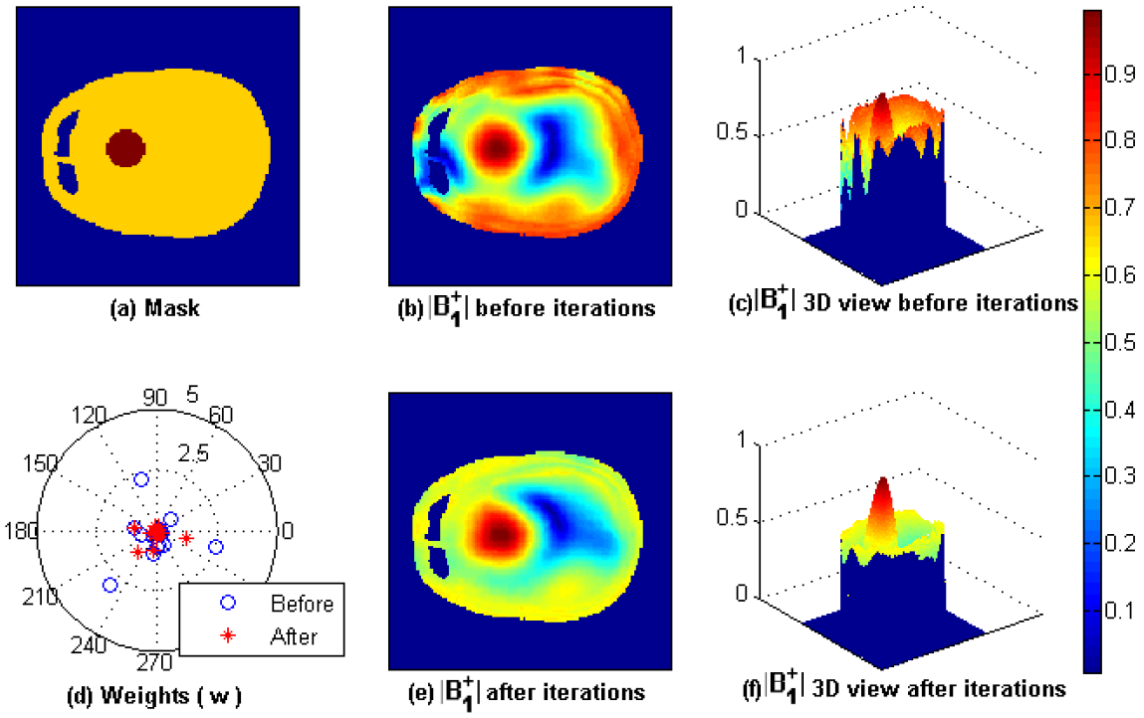

Figure 4.4: Finite Difference Time Domain Human Head Model Results at 9.4T (400MHz) when the 16 channel head coil is used. (a) A head model mask and ROI is shifted to the left. (b)-(c)$\left|B_1^+\right|$ result with initial convex optimizations. (d) The blue and red marks represent amplitudes and phases applied to the driven ports before and after iterations, respectively. (e)-(f) $\left|B_1^+\right|$ results after applying the iterative method.

region of interest located at the left, the opposite location has a relatively low $\left|B_1^+\right|$ field (Fig. 4.4(b) and 4.4(e)). As the target moves to the edge, this lack of symmetry become apparent and more channel coil elements may be required to produce good SNR images. The details are discussed in the phantom model simulations.

4.3.2 9.4T vs. 7T B_1^+ Fields Inhomogeneity

As magnetic field strengths increase, more inhomogeneous B_1 fields are expected due to higher interference in the human tissue. In particular, when a multi-channel head coil with

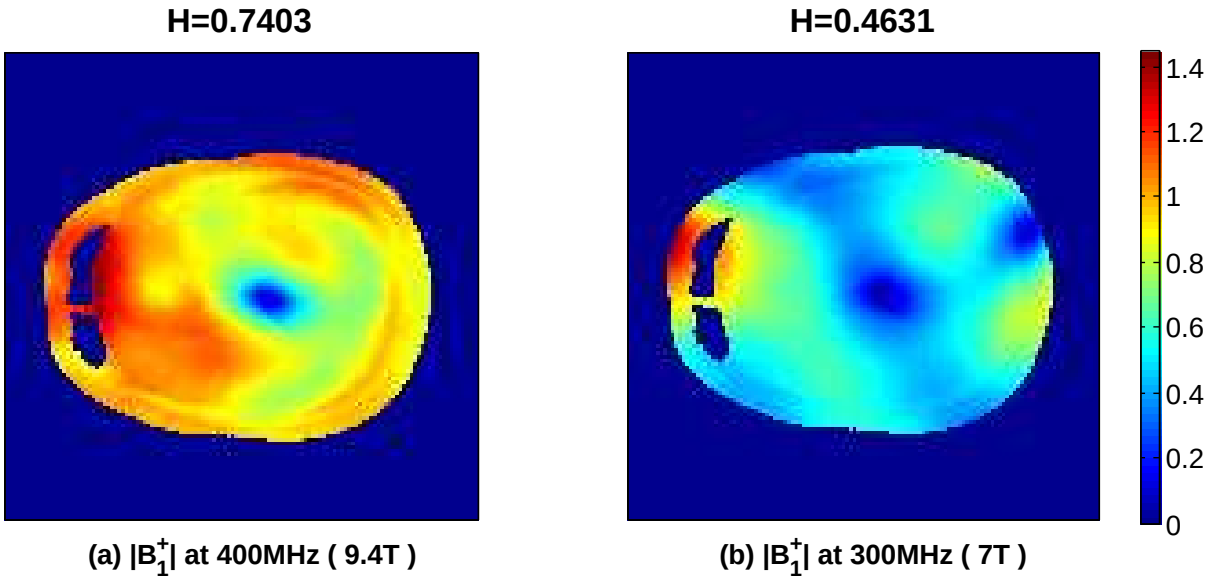

Figure 4.5: $\left|B_1^+\right|$ simulated results when all weights are unity $w_1 = w_2 = \cdots = w_{16} = 1$. **H** is a homogenous coefficient in the whole region.

the same amplitude and phase for each element of the coil is impressed, the difference in homogeneity is observed in the simulated $\left|B_1^+\right|$ results (Fig. 4.5). For instance, the weakest $\left|B_1^+\right|$ area the blue-colored in 7T simulations is much larger than it in 9.4T simulations. In addition, in terms of the homogeneous coefficient, the 9.4T $\left|B_1^+\right|$ result is 38% less homogeneous than the simulated 7T $\left|B_1^+\right|$ results. This lower homogeneity in the 7T system means the target region (region of interest) may be larger with convex optimization. Compared to 9.4T simulations in Fig. 4.2-4, Fig. 4.6 verifies this property, which should be considered when the target size is selected. The detailed comparison of the target size is tabled by counting the number of pixels in the ROI (Table 4.1). Table 4.1 shows that the number of pixels for 7T is almost doubled the number of pixels for 9.4T for each case. These findings explain that lower field strength systems can provide the larger region of interest, in particular for the B_1^+ field distribution in the head.

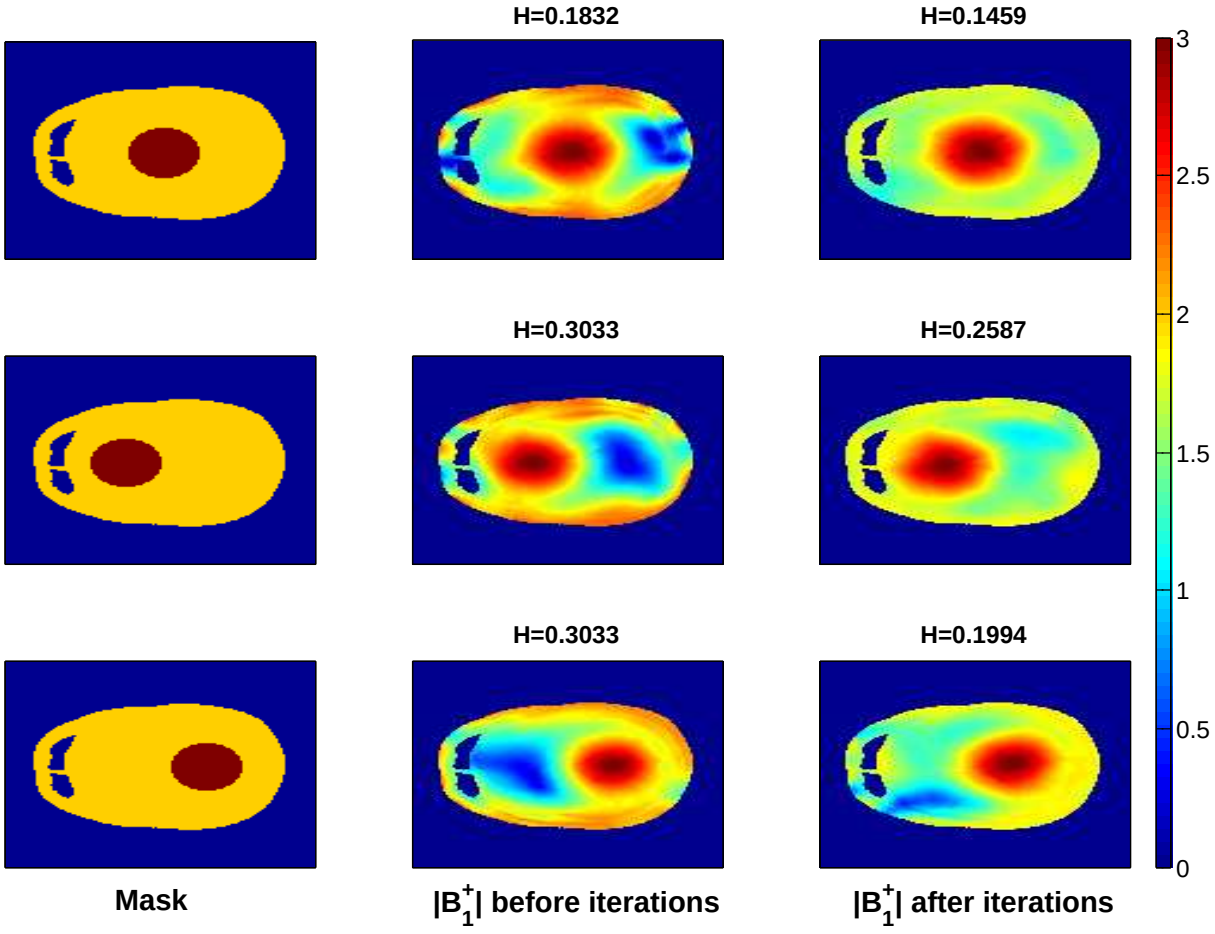

Figure 4.6: Finite Difference Time Domain Human Head Model Results at 7T (300MHz) when the 16 channel head coil is used. The comparison of $\left|B_1^+\right|$ results before and after iterations with 3 different target regions. The relatively larger target regions in the 7T simulations are apparent.

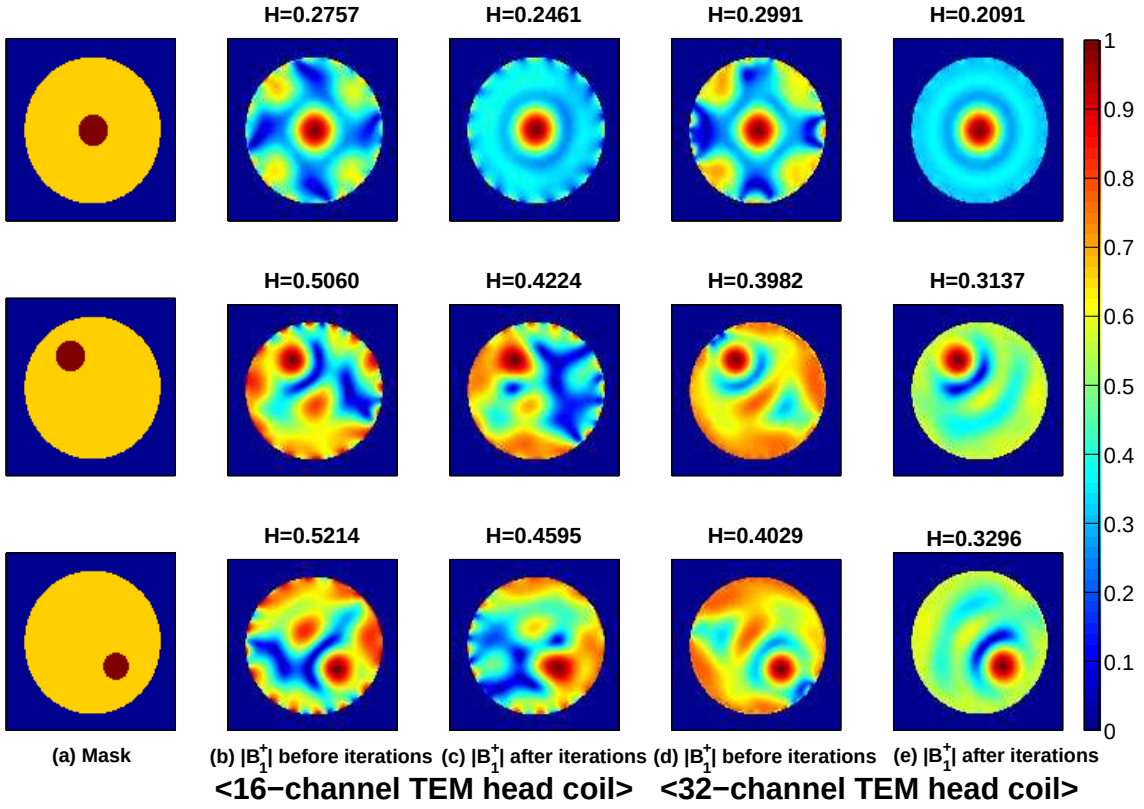

Figure 4.7: Finite Difference Time Domain Results at 9.4T (400MHz) in a phantom model. The 16-channel ((b), (c)) and 32-channel TEM head coil ((d), (e)) are driven. The comparison of $\left|B_1^+\right|$ results before and after iterations with 3 different ROI. Note that more homogeneous suppression regions in the 32-channel simulations are obtained.

	ROI is at the center		ROI is off center	
The value of $\|B_1^+\|$	9.4T	7T	9.4T	7T
$\|B_1^+\| > 0.95$	63	112	68	130
$\|B_1^+\| > 0.90$	141	274	146	270
$\|B_1^+\| > 0.85$	223	458	242	432
$\|B_1^+\| > 0.80$	323	634	339	606
$\|B_1^+\| > 0.75$	425	831	452	797
$\|B_1^+\| > 0.70$	530	1047	572	1022
$\|B_1^+\| > 0.65$	658	1298	720	1590

Table 4.1: Comparison the number of pixels in the ROI between 9.4T and 7T systems through the human head model. The total number of pixels in the human head mask is 6710. The calculations were performed using the FDTD model where the maximum value of $\left|B_1^+\right|$ in the slice is set to 1 at the center of ROI.

4.3.3 Phantom Model

A 3-liter sphere with relative permittivity of 80 and conductivity of 1.17 Siemens/m is used as the phantom model for simulations. The phantom model simulations are performed to enhance convex optimization with an iteration and compare a 16-element with a 32-element coil at 9.4T. Similar to the human head model, the axial slices of the center of phantom are used for the simulations. The phantom studies are different from the head model as the phantom is perfectly symmetry. This symmetry enables further investigation of the channel coil.

In this section, 16-channel element coil is compared to the 32-channel at 9.4T systems. Fig. 4.7 illustrates the $\left|B_1^+\right|$ field distributions depending on the position of ROI and compares the results from the 16 and 32 channel coil. In this analysis, three positions of ROI

are chosen and for simplicity, each ROI is a circle (Fig. 4.7(a)). To solve convex formulation in (4.2), $B^+_{1,c}$ is defined at the center of the ROI, and initial $B^+_{1,s}$ fields contain all B^+_1 except in the ROI. With this fields choice, the simulation results have poor homogeneity, especially when the ROI is located near the edges with 16-channel coil excitations (Fig. 4.7(b)). Applying the iterative method, $B^+_{1,s}$ fields are modified by eliminating B^+_1 gradually near the outer boundary of the ROI. Even though Fig. 4.7(c) shows homogeneity improvements by about 15%, more homogeneity is required for the ROI near the edge. To overcome this problem, a 32-channel head coil was used since larger number of channels equate to lower dependence on geometry. Comparing 16-channel and 32-channel FDTD results, the 32-channel homogeneity is much better compared to the 16-channel coil for all positions of ROI. The homogeneity coefficient is also reduced by approximately 25-30% with the iterative method (Fig. 4.7(c),(e)).

4.4 Hardware Setup

This chapter documents the 9.4T hardware setup[1] before the experimental results are discussed. Vaughan *et al.* [38] also document this 9.4T system with the preliminary results on it.

4.4.1 Magnet

As shown Fig 4.8, the super conducting solenoidal magnet is Magnex Scientific 9.4T with 65cm bore diameter. The operating current is 218 Amps with 78 MJ of stored energy. Cryostat height and length are 3.48 and 3.14 meter, respectively. Total conductor length is 354km.

[1]The related figures provided by the Center for Magnetic Resonance Research (CMRR).

Figure 4.8: Magnex Scientific Limited 9.4Tesla/65cm bore

4.4.2 Magnet legs

To accommodate the multi-channel antenna for the parallel imaging, "magnet leg" containing pre-amps, T/R switch, and mixers is used. Since each magnetic leg has 4 channels, four magnetic legs are required to use the 16 channel coil (Fig. 4.9).

4.4.3 Power Amplifiers

Sixteen 500-W broadband RF power amplifiers feed the multi-channel RF coil. RF power monitor interface boards are in place for satety shutdown.

4.4.4 Phase and Gain Controller

After setting the multi-channel system, phase and gain of each channel coil need to be controlled to generate signals. In particular, the field localization requires this controller to

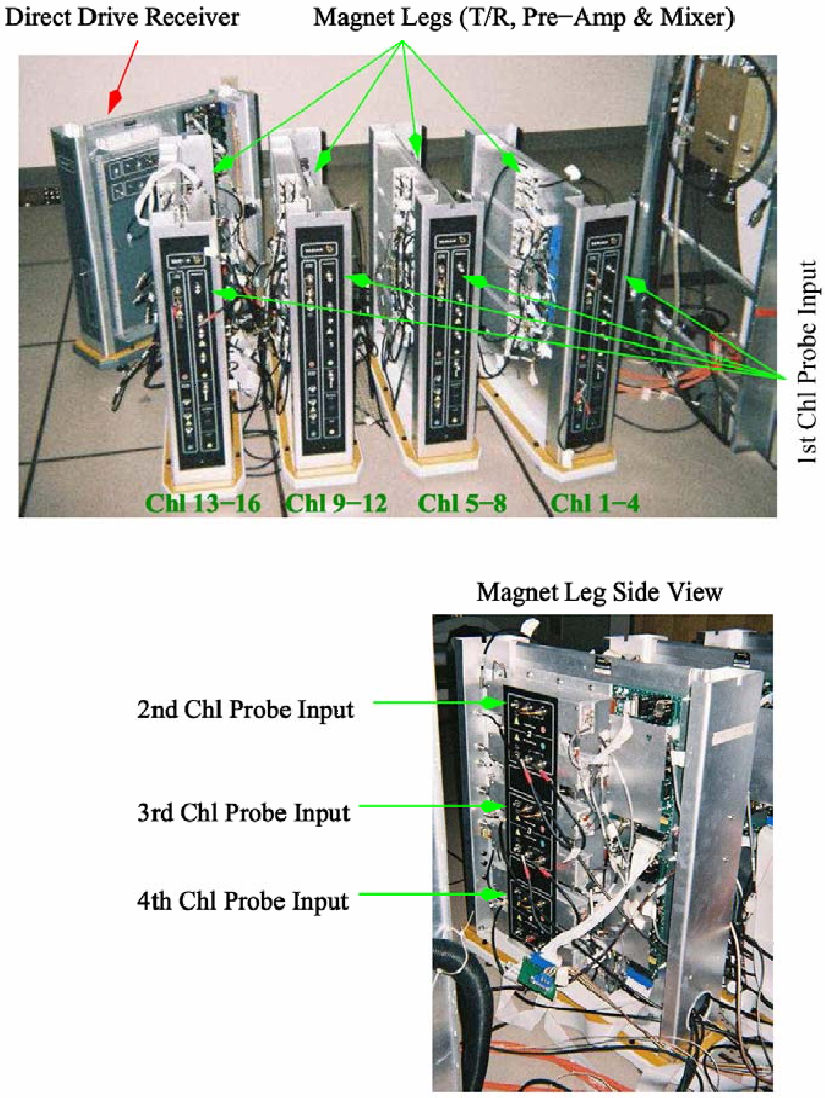

Figure 4.9: 9.4T 65cm Magnet legs

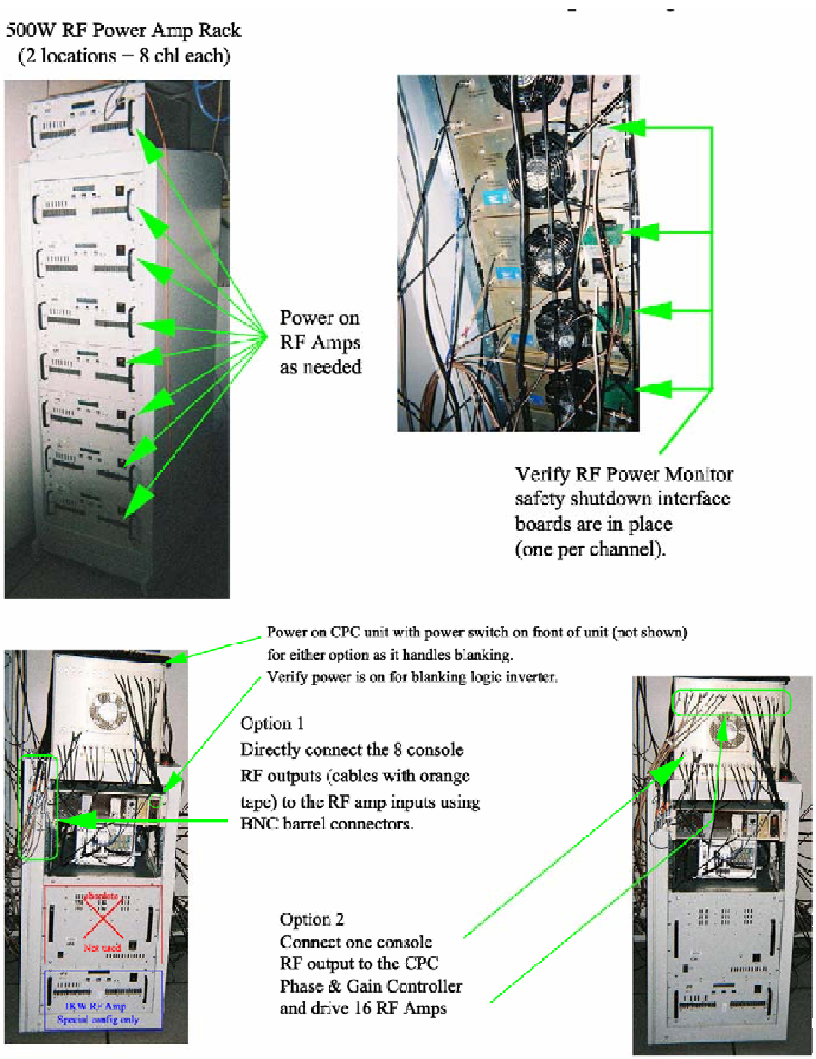

Figure 4.10: 500-W RF power amplifiers (top view), phase and gain controller (bottom view)

shift and attenuate the output signal from amplifiers. Phase and gain controller is managed by "DirectDrive" or "CPC unit" as shown in Fig. 4.10.

4.4.5 Multi channel Coils

A lot of different multi-channel coils are shown in Fig. 4.11[2]. In this study, eight-stripline coil is used. Since these multi-channel TEM coils are very sensitive to loads, matching a resonant frequency is critical to provide good quality images.

4.5 Experimental Results

For demonstration, an experiment was performed using an 8-channel TEM head coil at the 9.4T, 65 cm diameter bore system with an asymmetric 40 cm diameter head gradient and shim set [38]. The phantom consists of a spherical container of 99mM NaCl solution in water and its diameter is about 15cm. The magnitude of B_1^+ can be easily obtained with the conventional double angle method (DAM), whereas the correct phase information is difficult to find. To overcome this problem, the relative phase mapping method [50] is applied to set both magnitude and phase of B_1^+ after having $\left|B_1^+\right|$ by DAM. An axial slice in the center of the phantom was investigated with the Gaussian RF pulse and general parameters were: matrix = 128×128, FOV = 20cm×20cm, and slice thickness = 5mm. For $\left|B_1^+\right|$, TR/TE=2.5s/4ms and $\theta_1/\theta_2 = 45°/90°$. For $\angle B_1^+$, TR/TE=40ms/4ms and a flip angle =90°. In Fig. 4.12, $\left|B_1^+\right|$ fields are obtained for three different ROI after convex optimization with the iterative method. Note that the selection of ROI is limited by the geometric setting of phantom in the 8-channel transmission line head coil. This limitation will be solved when the 16- or 32-channel transmission line head coil is implemented.

[2]Multi channel coil pictures provided by Carl Snyder.

Figure 4.11: Multi-channel Transmission Line (TEM) Coils

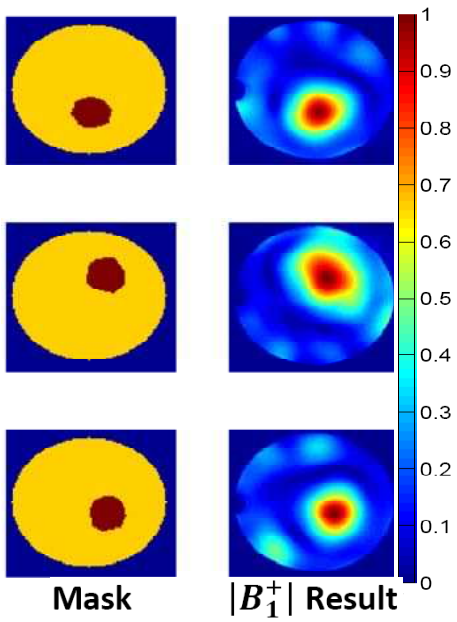

Figure 4.12: Experimental Results at 9.4T (400MHz) in a phantom model. Measured $\left|B_1^+\right|$ is obtained for three different ROI after convex optimization with the iterative method.

Chapter 5

Conclusion and Future Work

5.1 Conclusion

Three different methods which the combined the finite-element with boundary integral equations are used to evaluate the dispersion characteristics of open boundary structures in Chapter 2. First, an iterative method with the singular value decomposition is used with the wave equation and the boundary condition matrices. The technique has been demonstrated excellent accuracy for the evaluation of β for a rectangular dielectric waveguide. The zero cutoff of the lowest order mode has also been obtained. Next, to reduce computation time by avoiding iterations, the penalty function method was used to find the propagation constant β of open dielectric waveguides. This method provides good agreement with previous publications and has the advantage of eliminating spurious solutions by using edge elements, and no iterations are required after a suitable penalty factor has been determined. Finally, a pseudoinverse method using a combination of the finite-element method with boundary integral equation with a penalty factor, has been developed to obtain the solutions of propagating modes of open dielectric waveguides. This method has been demonstrated

to have results that compare very well with previous published ones, and also obtains simultaneous solutions of the various modes of a rectangular dielectric waveguide.

The electromagnetic scattering problem by arbitrary objects is discussed based on the method of moments technique solution of the combined field integral equations. Similar to the case of the conducting scatterers, the arbitrary geometrical shapes have been modeled by triangulated patches when combined field integral formulations are developed for the scattering by dielectric objects. The treatment of singularities in these solutions is discussed and the results for the metal plate are compared with earlier publications. The approach is applied to the scattering problem of a plane wave incident on a dielectric finite circular cylinder and a cubic high dielectric resonator. Scattered fields are evaluated after determining the surface electric and magnetic currents as unknowns for the high dielectric cube. The verification of the existence of the magnetic and electric dipole inside the cubic high dielectric resonator will be very useful in metamaterial applications.

High field MRI systems lead to image non-uniformity since the wavelength in the head becomes shorter than its size. To overcome this, in this study, RF field localizations through convex optimization with an iterative method was performed on both the human head and phantom models with operating frequencies 300 MHz for the 7T MRI system and 400 MHz for the 9.4T MRI system to design coil channel excitation parameters which result in good signal to noise ratios in the region of interest. Although the previous convex optimization without iterations generates large signals in the target region, the poor homogeneity was a problem in the suppression region. By applying the iterative method to the convex optimization, however, more homogeneous B_1^+ fields are obtained in the suppression region for both 9.4T and 7T systems. Simulations and experimental results show homogeneous images in regions of interest obtained after the proposed method was implemented. Variations with

the number of elements and different regions of interest have also been discussed.

5.2 Future Research Direction

Chapter 2 of the thesis has proposed three different methods to analyze open dielectric waveguides using the finite element method and boundary integral equations. Even though these methods have good agreement with the previous publications, each method has the disadvantages such as requiring iterations, depending on the penalty factor, and cutoff of the lowest mode. Therefore, the ultimate new method needs to be investigate to have all advantages of each proposed method.

The method of moments for the electromagnetic scattering problem by arbitrary shaped homogeneous dielectric objects is discussed in Chapter 3. To make this method more valuable in MRI applications, the antenna coil feeding model must be designed and analyzed numerically instead of excition by a plane wave. Then, faster solutions can be obtained compared to the finite difference time domain solver. To reduce the computation time, the single integral equation method for dielectric scatterers may be used because the combined integral equation formulation generally needs increased computation time and storage requirement. [51] may be a solution for the scattering problem in the MRI application.

Human head localizations have not measured in this thesis. Due to the limited time between patient movements, a faster B_1 mapping technique over the double angle method (DAM), which needs relatively long time for B_1 map acquisition, have to be developed. In addition, the safety of the RF power levels in the high magnetic field systems must be concern for further studies on human subjects. In addition, fast RF impedance matching network between multi-channel coils and RF power amplifiers is required to hold a fixed

resonant frequency because these coils are very sensitive to loads inside and outside.

Bibliography

[1] C. G. Williams and G. K. Cambrell, "Numerical solution of surface waveguide modes using transverse field components," *IEEE Transactions on Microwave Theory Techniques*, vol. 22, no. 3, pp. 329–330, March 1974.

[2] E. A. J. Marcartili, "Dielectric rectangular waveguide and directional coupler for integrated optics," *Bell Syst. Tech. J.*, vol. 53, no. 53, pp. 2071–2102, September 1969.

[3] J. E. Goell, "A circular-harmonic computer analysis of rectangular dielectric waveguides," *Bell Syst. Tech. J.*, vol. 48, no. 48, pp. 2133–2160, September 1969.

[4] C. C. Su, "Surface integral equations method for homogeneous optical fibers and coupled image lines of arbitrary cross-sections," *IEEE Transactions on Microwave Theory Techniques*, vol. 33, no. 11, pp. 1114–1119, November 1985.

[5] C. C. Su, "A combined method for dielectric waveguides using the finite-element technique and the surface integral equations method," *IEEE Transactions on Microwave Theory Techniques*, vol. 34, no. 11, pp. 1140–1146, November 1986.

[6] K. Hayata, M. Koshiba, M. Eguchi, and M. Suzuki, "Novel finite-element formulation without any spurious solutions for dielectric waveguides," *Electronics Letters*, vol. 22, pp. 295–296, March 1986.

[7] H. Rogier, F. Olyslager, and D. D. Zutter, "A hybrid finite element integral equation approach for the eigenmode analysis of complex anisotropic dielectric waveguides," *Radio Science*, vol. 31, pp. 999–1010, July 1996.

[8] M. V. Eliseev, A. G. Rozhnev, and A. B. Manenkov, "Guided and leaky modes of complex waveguide structures," *Journal of Lightwave Technology*, vol. 23, no. 8, pp. 2586–2594, August 2005.

[9] K. Okamoto, *Fundamentals of optical waveguides*. Academic Press, 2005.

[10] H. Yoo, Y. Boubendir, and A. Gopinath, "Analysis of open waveguides using the finite-element method and boundary integral equations," *IEEE Journal of Quantum Electronics*, vol. 44, no. 7, pp. 676–679, July 2008.

[11] H. Yoo and A. Gopinath, "Analysis of open dielectric waveguides using the finite-element penalty method," *Optics Letters*, vol. 33, no. 18, pp. 2068–2070, September 2008.

[12] H. Yoo and A. Gopinath, "Pseudoinverse method for modal solutions of open dielectric waveguides," *Optics Letters*, vol. 34, no. 8, pp. 1282–1284, April 2009.

[13] J. F. Lee, D. K. Sun, and Z. J. Cendes, "Full-wave analysis of dielectric waveguides using tangential vector finite elements," *IEEE Transactions on Microwave Theory Techniques*, vol. 39, no. 39, pp. 1262–1271, August 1991.

[14] P. P. Silvester and R. L. Ferrari, *Finite elements for electrical engineers.* Cambridge Univ. Press, 1983.

[15] J. Jin, *The finite element method in electromagnetics.* Wiley, 2005.

[16] R. F. Harrington, *Field computation by moment methods.* IEEE Press, 1993.

[17] C. A. Balanis, *Advanced engineering electromagnetics.* Wiley, 1989.

[18] Z. Abid, K. Johnson, and A. Gopinath, "Analysis of dielectric guides by vector transverse magnetic field finite elements," *Journal of Lightwave Technology*, vol. 11, no. 10, pp. 1545–1549, October 1993.

[19] B. M. A. Rahman and J. B. Davies, "Penalty function improvement of waveguide solution by finite elements," *IEEE Transactions on Microwave Theory Techniques*, vol. 32, no. 8, pp. 922–928, August 1984.

[20] M. Silveira and A. Gopinath, "Analysis of dielectric guides by transverse magnetic field finite element penalty method," *Journal of Lightwave Technology*, vol. 13, no. 3, pp. 442–446, March 1995.

[21] P. Cheung, M. Silveira, and A. Gopinath, "Correction to the analysis of dielectric guides by transverse magnetic field finite element penalty function method with extenstions," *Journal of Lightwave Technology*, vol. 14, no. 12, pp. 2799–2803, December 1996.

[22] S. M. Rao, *Electromagnetic scattering and radiation of arbitrarily shaped surfaces by triangular patch modeling.* Ph.D. dissertation, University of Mississippi, 1980.

[23] K. Umashankar, A. Taflove, and S. M. Rao, "Electromagnetic scattering by arbitrary shaped three-dimensional homogeneous lossy dielectric objects," *IEEE Transactions on Antennas and Propagation*, vol. 34, no. 6, pp. 758–766, June 1986.

[24] R. D. Graglia, "On the numerical integration of the linear shape functions times the 3-D Green's functions or its gradient on a plane triangle," *IEEE Transactions on Antennas and Propagation*, vol. 41, no. 10, pp. 1448–1455, October 1993.

[25] P. Yla-Oijala and M. Taskinen, "Calculation of CFIE impedance matrix elements with RWG and $n\times$ RWG functions," *IEEE Transactions on Antennas and Propagation*, vol. 51, no. 8, pp. 1837–1845, August 2003.

[26] R. E. Hodges and Y. Rahmat-Samii, "The evaluation of MFIE integrals with the use of vector triangle basis functions," *Microwave and Optical Technology Letters*, vol. 14, no. 1, pp. 9–14, January 1997.

[27] C. L. Holloway, E. F. Kuester, J. Baker-Jarvis, and P. Kabos, "A double negative (DNG) composite medium composed of magnetodielectric spherical particles embedded in a matrix," *IEEE Transactions on Antennas and Propagation*, vol. 51, no. 10, pp. 2596– 2603, October 2003.

[28] L. Jylha, I. Kolmakov, S. Maslovski, and S. Tretyakov, "Modeling of isotropic backward-wave materials composed of resonant spheres," *Journal of Applied Physics*, vol. 99, p. 043102, 2006.

[29] L. Peng, L. Ran, H. Chen, H. Zhang, J. A. Kong, and T. M. Grzegorczyk, "Experimental observation of left-handed behavior in an array of standard dielectric resonators," *Physical Review Letters*, vol. 98, no. 15, p. 157403, 2007.

[30] J. Kim and A. Gopinath, "Simulation of a metamaterial containing cubic high dielectric resonators," *Physical Review B*, vol. 76, no. 11, p. id. 115126, September 2007.

[31] J. Kim, *Design, characterization, and application of metamaterial using high dielectric resonators*. Ph. D.'s thesis, University of Minnesota, 2008.

[32] S. M. Rao, D. R. Wilton, and A. W. Glisson, "Electromagnetic scattering by surfaces of arbitrary shape," *IEEE Transactions on Antennas and Propagation*, vol. 30, no. 3, pp. 409–418, May 1982.

[33] A. H. Stroud, *Approximate calculation of multiple integrals*. Prentice Hall, 1971.

[34] Y. Kamen and L. Shirman, "Triangle rendering using adaptive subdivision," *IEEE Computer Graphics and Applications*, vol. 18, no. 12, pp. 95–103, March 1998.

[35] M. F. Catedra, J. G. Cuevas, and L. Nuno, "A scheme to analyze conducting plates of resonant size using theconjugate-gradient method and the fast Fourier transform," *IEEE Transactions on Antennas and Propagation*, vol. 36, no. 12, pp. 1744–1752, December 1988.

[36] C. A. Balanis, *Antenna theory*. Wiley, 1982.

[37] J. Vaughan, M. Garwood, C. Collins, W. Liu, L. DelaBarre, G. Adriany, P. Anderson, H. Merkle, R. Goebel, M. Smith, and K. Ugurbil, "7T vs. 4T: RF power, homogeneity and signal to noise comparison in head images," *Magnetic Resonance in Medicine*, vol. 46, pp. 24–30, July 2001.

[38] J. Vaughan, L. DelaBarre, C. Snyder, J. Tian, C. Akgun, D. Shrivastava, W. Liu, C. Olson, G. Adriany, J. Strupp, P. Anderson, A. Gopinath, and P.-F. Moortele, "9.4T human MRI: Preliminary results," *Magnetic Resonance in Medicine*, vol. 56, pp. 1274–1282, October 2006.

[39] J. Vaughan, *RF coil for imaging system.* U.S. patent 6,633:161, 2003.

[40] S. Wang, J. Murphy-Boesch, H. Merkle, A. Koretsky, and J. Duyn, "B_1 homogenization in MRI by multilayer coupled coils," *IEEE Trans. Medical Imaging*, vol. 28, no. 4, pp. 551-554, 2009.

[41] R. Abraham and T. Ibrahim, "Proposed radiofrequency phased-array excitation scheme for homogenous and localized 7-Tesla whole body imaging based on full-wave numerical simulations," *Magnetic Resonance in Medicine*, vol. 57, pp. 235-242, 2007.

[42] T. Ibrahim, C. Mitchell, P. Schmalbrock, R. Lee, and D. Chakeres, "Electromagnetic perspective on the operation of RF coils at 1.5-11.7 Tesla," *Magnetic Resonance in Medicine*, vol. 54, pp. 683-690, 2005.

[43] T. Ibrahim, R. Lee, B. Baertlein, A. Abduljalil, H. Zhu and P. Robitaille, "Effect of RF coil excitation on field inhomogeneity at ultra high fields: A field optimized TEM resonator," *Magnetic Resonance in Medicine*, vol. 19, pp. 1339-1347, 2001.

[44] B. Li, F. Liu, and S. Crozier, "Focused, eight-element transceive phased array coil for parallel magnetic resonance imaging of the chest," *Magnetic Resonance in Medicine*, vol. 53, pp. 1251–1257, May 2005.

[45] S. Boyd and L. Vandenberghe, *Convex optimization.* Cambridge University Press, 2004.

[46] C. Olson, *RF field localization in magnetic resonance imaging.* Master's thesis, University of Minnesota, 2007.

[47] H. Yoo, J. Vaughan, and A. Gopinath, "Convex optimization with iterations for RF B_1 field localization in 9.4T MRI system," in *Applied Computational Electromagnetics Society*, Monterey, USA, March 2009.

[48] C. Collins and M. Smith, "Signal-to-noise ratio and absorbed power as functions of main magnetic field strength, and definition of "90°" RF pulse for the head in the birdcage coil," *Magnetic Resonance in Medicine*, vol. 45, pp. 684–691, March 2001.

[49] M. Grant and S. Boyd, *CVX: Matlab software for disciplined convex programming.* http://stanford.edu/ boyd/cvx, 2007.

[50] P.-F. Moortele, C. Akgun, G. Adriany, S. Moeller, J. Ritter, C. Collins, M. Smith, J. Vaughan, and K. Ugurbil, "B_1 destructive interferences and spatial phase patterns at 7T with a head transceiver array coil," *Magnetic Resonance in Medicine*, vol. 54, pp. 1503–1518, November 2005.

[51] M. S. Yeung, "Single integral equation for electromagnetic scattering by three-dimensional homoegenous dielectric object," *IEEE Transactions on Antennas and Propagation*, vol. 47, no. 10, pp. 1615–1622, October 1999.